2013

Inelastic neutron scattering studies of magnetic fluctuations in the tetragonal and collapsed tetragonal phases of $CaFe_2As_2$

Jing Han Soh
Iowa State University

Inelastic neutron scattering studies

of magnetic fluctuations in the tetragonal and collapsed tetragonal phases of

$CaFe_2As_2$

by

Jing Han Soh

A thesis submitted to the graduate faculty

in partial fulfillment of the requirements for the degree of

MASTER OF SCIENCE

Major: Condensed Matter Physics

Program of Study Committee:

Alan I. Goldman, Major Professor

Robert J. McQueeney

Lee Anne Willson

Duane Johnson

Iowa State University

Ames, Iowa

2013

TABLE OF CONTENTS

LIST OF TABLES

LIST OF FIGURES

ACKNOWLEDGEMENTS

I would like to take this opportunity to express my thanks to those who helped me with various aspects of conducting research and the writing of this thesis.

First and foremost, I have enormous gratitude for my advisor, Dr. Alan Goldman, for his guidance, patience and inspirational teaching style throughout this research and my graduate education in Ames. I am grateful to Dr. Robert McQueeney and would like to thank him for the clear insights with the inelastic neutron scattering experiment and analysis. I also learned a huge amount from Greg Tucker, and would like to thank him for his help with the analysis and the co-alignment of crystals. I have much gratitude for the constant support and guidance from Andreas Kreyssig.

I also owe thanks to the people I worked along with at Ames Laboratory and Iowa State University: Mingyu Kim and Daniel Pratt, who have guided me throughout my first experience in the group. Also, Dante Quirinale, Gus Rustan, Aashish Sapkota, Wageesha Jayasekara and Shree Ram Banjara who have made this experience enjoyable. I am grateful to Sheng for growing the single crystals used for this thesis, and to the instrument scientists, Matt Stone and Doug Abernathy at ARCS, who have helped me with the neutron scattering measurements. I especially want to thank all the scatterers for their encouragement over cups of coffee. Also, I would like to thank my committee members for their efforts and time commitment to this work: Dr. Lee Anne Wilson and Dr. Duane Johnson. I am grateful to my colleagues and staff at the Iowa State University Department of Physics and Astronomy.

Thank you also to my family in Iowa: Fritzie Rivas, Kristin Manibog, Mapi Faylon and Katrina Lutap. Last, but not least, I am grateful for my family especially my parents, my sister JingNi, Steve and Shirley Mellema for their constant support and love.

ABSTRACT

The relationship between magnetism and superconductivity has become a central topic of research in studies of superconductivity in the iron pnictides. This thesis presents inelastic neutron scattering studies of the magnetic excitations in FeAs flux-grown $CaFe_2As_2$. The experimental data collected using ARCS time-of-flight chopper spectrometer have been analyzed and compared with theoretical models. The focus here is on the role played by antiferromagnetic (AFM) spin fluctuations in superconductivity. We present unambiguous evidence of the absence of magnetic fluctuations in the non-superconducting volume collapsed tetragonal (cT) phase of $CaFe_2As_2$ via inelastic neutron scattering time-of-flight data, which is consistent with the view that spin fluctuations are a necessary ingredient for unconventional superconductivity in the iron pnictides. We demonstrate that the cT phase of $CaFe_2As_2$ is non-magnetic, raising new questions regarding recent reports of high-temperature superconductivity in the cT phase of closely related compounds.

CHAPTER 1. Introduction to iron-arsenide based superconductors

1.1 Introduction

Kamihara and co-workers reported superconductivity at T_C = 26 K in fluorine-doped LaFeAsO.[10] Reports of higher T_C immediately followed with a variety of doping for Fe, as well as the replacement of lanthanum with rare earth ions of smaller atomic radii, and the application of pressure.[11, 12, 13] An iron-arsenide-based superconductor was first found in the tetragonal compound LaFePO with a superconducting temperature of $T_C \sim 4$ K. The tetragonal crystal structure consists of alternating lanthanum oxide ($La^{3+}O^{2-}$) and iron pnictide ($Fe^{2+}P^{3-}$) layers, reminiscent of the layered structure found in the high-T_C cuprate superconductors.[14] Further study of the iron-pnictide compounds by the same Japanese group, revealed that the doping of F^- into the oxygen sites of the related compound, LaFeAsO, superconductivity with a highest midpoint T_C of 26 K.[10] This new class of high temperature superconductor generated much interest due to the presence of iron, which is magnetic, along with the high superconducting transition temperature.

Discoveries of cuprates and iron-arsenide superconductors have led to extensive research, largely because of their high superconducting transition temperatures which exceed the values predicted by BCS theory.[15, 16] It was initially thought that the magnetic nature of iron would disrupt the pairing of superconducting electrons and therefore destroys superconductivity. However, the high superconducting temperatures in this class of material proved otherwise. The electron-phonon coupling constant was found to be smaller than from experimentally measured T_C indicating that there are other coupling effects that induces superconductivity.[17] Even higher transition temperatures were recorded with the application of pressure ($T_C \sim$43 K [13]) and the substitution of La by other magnetic rare earth ions such as Sm ($T_C \sim$ 55 K

[18]) and Gd ($T_C \sim 56$ K [19]).

Iron-based superconductors contain either pnictide (group 15: P, As) or chalcogenide (group 16: S, Se, Te) layers (highlighted layer in Figure 1.1). There are four main iron-based family structures, denoted by their chemical family, e.g., 11,111, and 122 with different spacers between the common layers of FeAs (or FeSe). Superconductivity is thought to originate within the Fe-layers, similar to the CuO layers in cuprate superconductors. However, they differ in that the iron superconductors allow doping directly into the active layers, while superconductivity in cuprates is destroyed when dopants are introduced in the CuO layers.

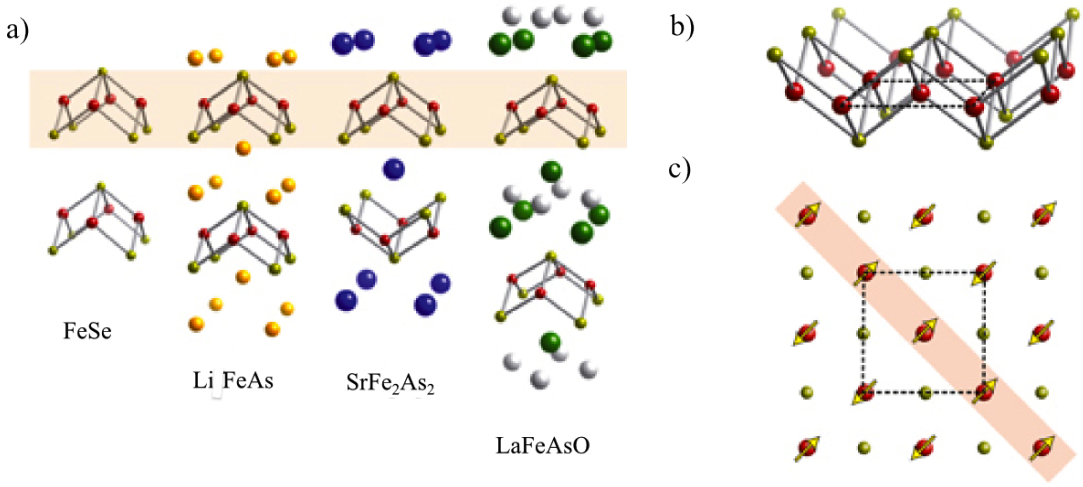

Figure 1.1 a) Crystal Structures of FeSe (11), LiFeAs (111), $BaFe_2As_2$ (122), and LaFeAsO (1111) iron based superconductors. When compared, the larger the separation of FeAs layers, the higher the superconducting transition temperature. (b)The FeAs/FeSe layer. Iron ions shown in red and pnictogen/chalcogen anions shown in gold. c) View from the top (c-axis) of the FeAs layer. The dashed line indicates the size of the unit cell of the FeAs-type slab, which includes two iron atoms and the ordered spin arrangement for FeAs-based materials is indicated by arrows.[1]

As there is not a conclusive theory regarding high-temperature superconductors, it is important to question the roles of crystal structures, structural phase transitions, dopants, pressure and magnetism in the occurrence of superconductivity. This chapter will present an overview of the current understanding of iron arsenide superconductors, with an emphasis $CaFe_2As_2$.

1.2 Structure and superconductivity in iron-arsenide superconductors

The LaFeAsO compound has a ZrCuSiAs-type structure (tetragonal, P4/nmm, space group No. 129) at room temperature with an FeAs layer bound by layers of LaO (See Figure 1.1).[20, 21] Superconductivity is realized by partial substitution of O^{2-} by F^{-} or Fe by Co. [10, 22] Substitution of La by other light rare-earth elements (Ce, Pr, Nd, Sm, Gd, Tb, and Dy) also induces superconductivity. The onset of the superconducting transition temperature increases with the decreasing size of the R (rare-earth) atoms.[23, 24] The family of RFeAsO (R=rare earth) superconductors with similar quaternary structure is denoted the 1111 family. Oxygen-deficient compounds ($ReFeAsO_{1-\delta}$) and electron doping by other rare earth substitutions (e.g. $Gd_{1-x}Th_xFeAsO$) also show superconductivity.[24, 19] Superconductivity was also found in the 111-type compound, LiFeAs, with T_C ∼18 K. LiFeAs crystallizes in a tetragonal PbFCl-type (P4/nmm) structure and it undergoes superconductivity in a purely stoichiometric compound without chemical doping.[25] Superconductivity was also reported in FeSe(11) compounds (α-PbO-type structure) with Se deficiency, application of pressure (T_C ∼27 K at 1.5 GPa) and substitution ($FeSe_{0.5}Te_{0.5}$) [26, 27]

The family of iron-pnictide being studied is the oxygen-free ternary 122-type MFe_2As_2 (M=Ca, Sr, Ba, Eu) and was first discovered in a potassium-doped $BaFe_2As_2$ parent compound ($T_C = 38$ K). The 122-family exhibits $ThCr_2Si_2$ crystal structure at room temperature.[28] It is the only class that does not have P4/nmm structure, but instead an $I4$/mmm structure (space group 139) due to the body-centered M atom shown in Figure 1.1. The 122 family has similar FeAs layers, but differs from the 1111 compound in that the interlayer contains only a single atom. Superconductivity in the 122 family can be achieved by doping at any of the three sites. The highest T_C attained was ∼38 K for $Ba_{1-x}K_xFe_2As_2$ [28], ∼20.5 K for $BaFe_{2-x}Ni_xAs_2$ [29] and ∼31 K for $BaFe_2(As_{1-x}P_x)$ [30]. After the discovery of K-doped $BaFe_2As_2$ and $SrFe_2As_2$, superconductivity was reported in $CaFe_2As_2$ with T_C ∼20 K via the substitution of Ca by Na.[5, 31].

1.3 $CaFe_2As_2$: case study of the 122-family

The absence of oxygen, or the required control of oxygen and fluorine stoichiometry, allows for large single crystals of 122-structure to be grown and studied extensively.[32] Iron-pnictide and cuprate superconductors are formed by doping their non-superconducting parent compounds. The parent phases of the 122-family are metallic compounds with the antiferromagnetic ordering strongly coupled to a structural transition. A representative phase diagram for 122-type is given in Figure 1.2.[2] At high temperature and ambient pressure, the compound is in paramagnetic and tetragonal phase. The antiferromagnetic (AFM) ordering appears below Néel temperature, (T_N). Doping suppresses the antiferromagnetic (AFM) orders in iron-arsenides, leading to superconductivity. Besides magnetic ordering, iron-arsenides also undergo a structural transition at T_S, from high-temperature tetragonal structure to a low-temperature orthorhombic phase. The two transitions happen at about the same temperature but clearly splits with doping. Doping also suppress the structural phase transition, leading to the onset of superconductivity. The highest T_C, only appears after the magnetic and structural transitions are completely suppressed.[4] At low temperature, there is a small doping (x) region where superconductivity co-exist with the AFM, orthorhombic structural distortion. The two states also competes with one another as seen with the bending back of the transition temperatures.

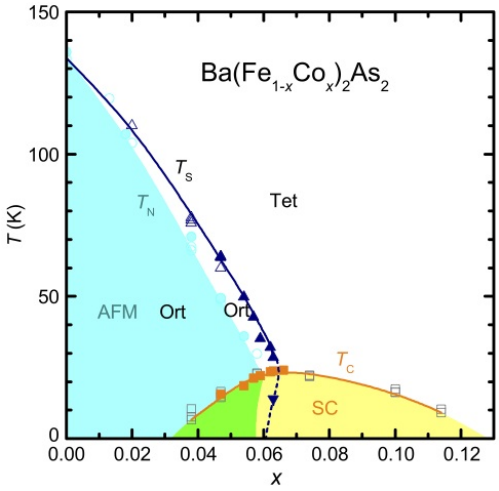

Figure 1.2 The temperature (T) versus doping (x) phase diagram of $Ba(Fe_{1-x}Co_x)_2As_2$ from reference [2]. The extension of the tetragonal-toorthorhombic phase line into the superconducting dome is represented by the dashed line.

1.3.1 Structural and magnetic transitions of $CaFe_2As_2$

Crystal Structure

$CaFe_2As_2$ compound is a body-centered tetragonal $ThCr_2Si_2$ crystal structure (I4/mmm, space group =139) at room temperature with lattice $a = b \neq c$ (Figure 1.3a). Single-crystal neutron diffraction of the compound at T = 300 K and ambient pressure shows a lattice constant of $a_T = 3.879(3)$ Å and $c_T = 11.740(3)$ Å.[33] Layers of Ca are located between two Fe-As tetrahedral layers. We observe two layers per unit cell, as the formula unit contains two M atoms. Neutron and x-ray diffraction studies show that the Ca-122 compound undergoes a first-order structural phase transition at a temperature, T_s ~173 K, from a high-temperature tetragonal unit cell to a low-temperature face-centered orthorhombic $Fmmm$ space group (Figure 1.3(b)) with $a \neq b \neq c$ (a_O= 5.506(2) Å, b_O= 5.450(2) Å, c_O= 11.66(6) Å at T=10 K).[5]

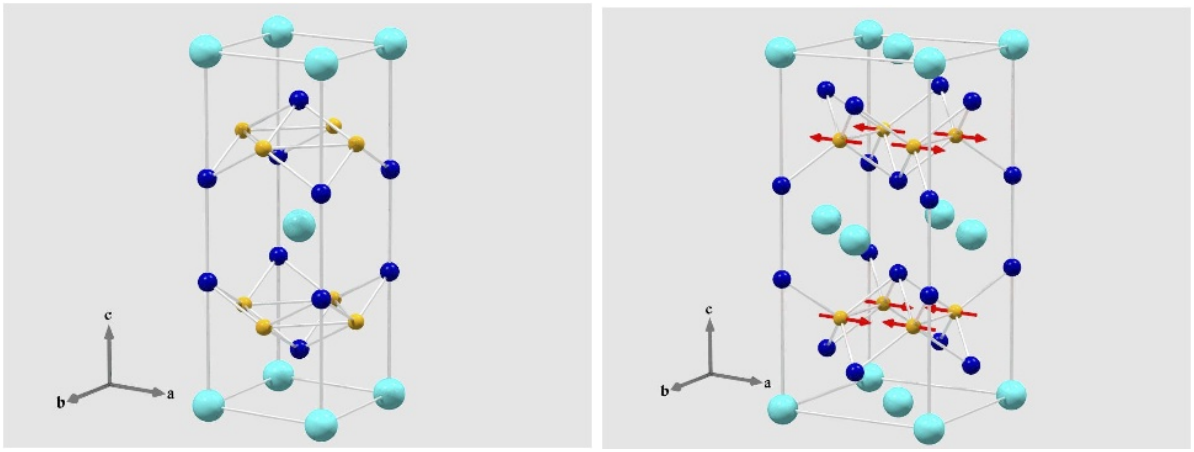

Figure 1.3 (Left) Tetragonal crystal structure of $CaFe_2As_2$ above T_S. The Ca atoms (light cyan) are located at the eight corners of the tetragonal unit cell and at the center, while four Fe atoms (gold) form a planar square lattice in the ab plane. Each Fe atom lies at the center of four As atoms (dark blue) to form tetrahedral $FeAs_4$. The volume collapsed-tetragonal (cT) phase has a similar crystal structure but with a 10 % reduced c lattice parameter. (Right) Antiferromagnetic structure of $CaFe_2As_2$ below T_S. The orthorhombic unit cell is the same as the magnetic cell. The Fe spins (red arrows) are oriented along the orthorhombic a axis. Figures are obtained from reference [3]

Magnetic structure

Magnetic structure refers to the orientation of spins in a magnetic material. Magnetic ions are distributed according to the periodicity of the crystal structure but the orientation of spins depends on the magnetic interaction between neighboring spins. In a paramagnet, there is an average site magnetization, which are correlated over short ranges but do not have net global magnetization(magnetic short-range order). At high enough temperature, all magnetic materials become paramagnetic, having no net magnetic moment. At low temperature, materials with long-range magnetic ordering can exhibit ferromagnetic (parallel spins) or antiferromagnetic (antiparallel spins) behavior depending on the spin correlations. As mentioned, $CaFe_2As_2$ compound undergoes a first-order structural phase transition at a temperature, T_s ~173 K, from a tetragonal unit cell to a face-centered orthorhombic space group. The structural transition is accompanied by antiferromagnetic ordering at a temperature T_N, at a close proximity to T_S. The magnetic transition temperature depends on the strength of exchange interactions and the magnetic moments.

The antiferromagnetic structure of $CaFe_2As_2$ below T_N can be seen in Figure 1.3. The orthorhombic unit cell is the same as the magnetic cell. For $CaFe_2As_2$, the collinear spins point along a_O. The magnetic moments are antiferromagnetically correlated along the $\boldsymbol{a_O}$ direction as indicated by the red arrows while the spins are ferromagnetically correlated along $\boldsymbol{b_O}$-axis (i.e., striped in the ab plane). The compound is also antiferromagnetic in the $\boldsymbol{c_O}$-direction. The close proximity of the magnetic (T_N) and structural (T_S) transition at $T \sim 172$ K indicates a strong connection between magnetic and structural transition.[33] The simultaneous structural and magnetic phase transitions are a common trend among the 122-type family (M=Sr[34], Ba[35]) and other families.

Scattering convention

The periodicity of atoms in crystal and the symmetry of lattices are important in investigating the properties of matter. Crystal structure can be determined from elastic scattering of

photons, neutrons and electrons. Bragg's diffraction law,

$$n\lambda = 2d\ sin\theta \tag{1.1}$$

illustrates a geometrical condition to be satisfied in order for constructive interference to occur between planes of atoms spaced by a distance, d where, n is an integer, λ is the wavelength of the incident wave, and θ is the angle between the incident wave and the scattering planes, or the Bragg angle. As diffraction patterns of crystals are Fourier transforms in wavevector space of the atomic positions in the material, it is related to the reciprocal lattice. The first Brillouin zone (BZ) of 122-type at room temperature is the body-centered-tetragonal (BCT). The reciprocal lattice of the real-space BCT (or direct) lattice is another BCT-lattice.[4] Figure 1.4 shows the planar view of 122-magnetic structure in real and reciprocal space.[3] The low-temperature orthorhombic basal plane a_O and b_O axes are rotated by 45° and the lattice parameters are a factor of $\sqrt{2}$ longer compared with the tetragonal lattice parameter a_T.

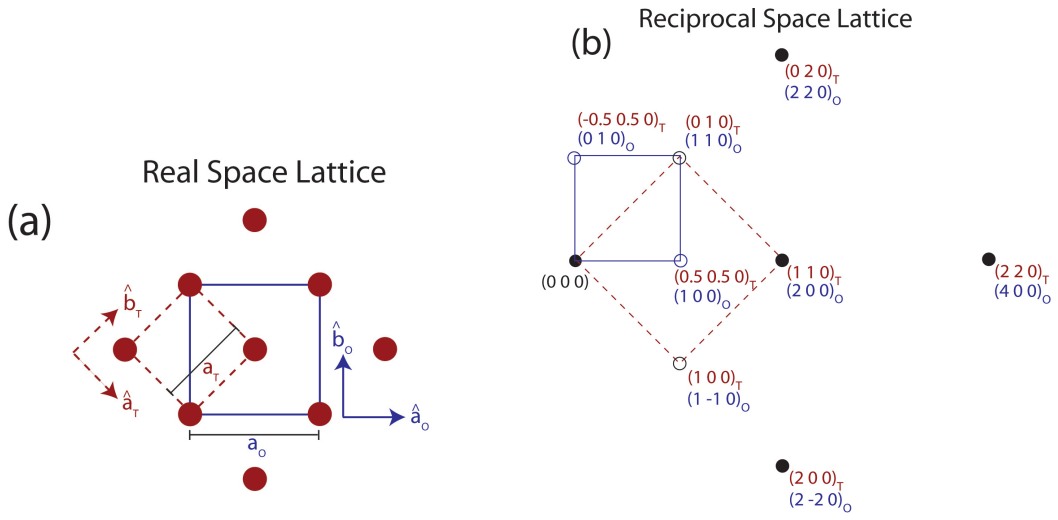

Figure 1.4 Planar view of the 122 magnetic structure in (a) real space and (b) reciprocal space. (a) The base of the tetragonal unit cell bounded by the brown dashed lines with lattice a_T ($a = b$). The orthorhombic cell is given by the blue solid lines with lattice a_O and b_O. (b) The reciprocal lattice associated with the square lattice in (a). The peaks for both tetragonal and orthorhombic notations are given. Figure is obtained from reference [3, 4].

The Bragg's relationship in Q-space gives Q = $\frac{4\pi}{\lambda}$ sin θ. A peak in the diffraction pattern

or reciprocal lattice space, occurs only if the wavevector $\mathbf{Q}$ satisfies,

$$\mathbf{Q} \;=\; h\mathbf{k_x} + k\mathbf{k_y} + l\mathbf{k_z} \tag{1.2}$$

where h,k, and l are the miller indices for the reciprocal lattice translation vectors $\mathbf{k_i}$ of the crystal. The h,k, and l values must be integers and h+k+l =even.[4] In this thesis, the positions in reciprocal space at wave vector $\mathbf{Q} = (Q_x, Q_y, Q_z)$ [$\mathring{A}^{-1}$] are described with the tetragonal $I4$/mmm unit cell, where $\mathbf{Q} = \frac{2\pi}{a}(H+K)\hat{i}+\frac{2\pi}{a}(H-K)\hat{j}+\frac{2\pi}{c}L\hat{k}$. The wavevector $\mathbf{Q}$ will be expressed in reciprocal lattice units $(H+K, H-K, L)$ (r.l.u) notation. The magnetic ordering vector for 122-compounds in tetragonal notation is $(\frac{h}{2}, \frac{k}{2}, l)_T$ but for orthorhombic reflections is $(h, 0, l)_O$ where h, k, and l are odd integers. Using this notation, the antiferromagnetic wave vector, $\boldsymbol{Q_{AFM}}$= $(\frac{1}{2}, \frac{1}{2}, L)$, for $H = \frac{1}{2}$, $K = 0$, and $L = odd$.

Suppression of structural and magnetic transition

The superconducting state in cuprate-based and iron-based superconductors is most easily induced by the chemical substitution of elements in the parent compound, which suppress the magnetic order and the structural distortions in favor of superconductivity. Doping with ions of various sizes changes the physical interatomic distance and dynamics between the layers (e.g. carrier concentration – hole or electron doping). K-doped $CaFe_2As_2$ has the highest T_C recorded for hole-doped Ca-122 superconductors at about ∼35 K.[36] The substitution of Fe by Co, or Ir or Rh under ambient pressure introduces superconductivity up to ∼22 K.[37, 38] In addition, electron doping of Ca-122 compounds by partially replacing Ca by rare-earth elements (Ce, Pr, and Nd) also appears to induce superconductivity, with the highest $T_C \sim 49$ K.[39] The evidence of the structural and magnetic transitions is given by discontinuities near 170 K in temperature-dependent resistivity, magnetic susceptibility and specific heat measurements made on single crystals grown from Sn flux.[5] Besides the discontinuities in the measurements, a hysteresis of several degrees can be seen in the thermodynamic, transport, and microscopic measurements. The signatures of the transitions can be seen in Figure 1.5 below. Both temperature-dependent electrical resistivity (a) and temperature-dependent magnetic susceptibility (b) of $CaFe_2As_2$ show a sharp jump near 170 K indicating a first-order phase transition.

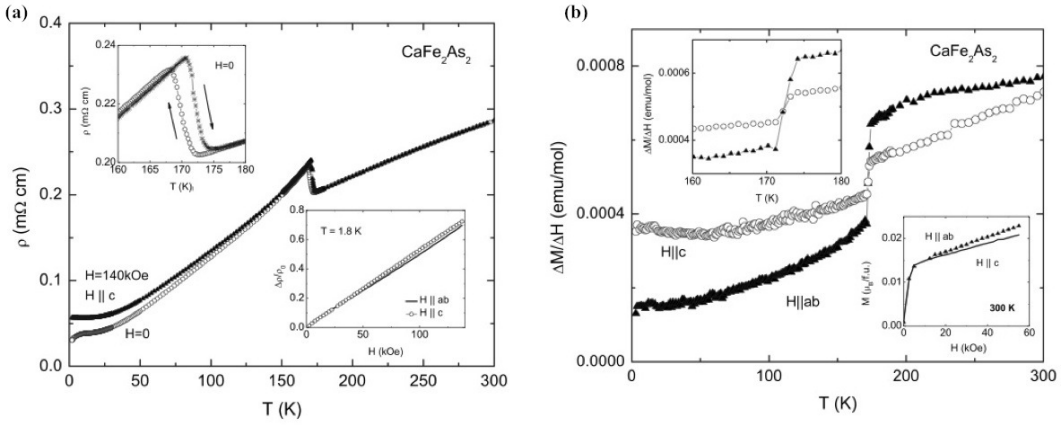

Figure 1.5 (a) Temperature-dependent electrical resistivity and (b) temperature-dependent magnetic susceptibility of $CaFe_2As_2$. A couple of representative result taken from reference [5].

Pressure studies

Besides doping, it was found that both copper-oxide and iron-based high-temperature superconductors manifest superconductivity when pressure is applied. Pressure-induced superconductivity enabled a systematic investigation into the FeAs superconductors without introducing any dopants, which inevitably changes the chemistry, introducing disorder to the compound. The application of a very modest hydrostatic pressure (P $<$ 5 kbar) suppress the magnetic ordering and structural phase transitions.[40] Torikachvili *et.al.* discovered that $CaFe_2As_2$ undergoes a high pressure (P $>$ 5.5 kbar) transition into a new phase that is detrimental to superconductivity. The highest T_C recorded was $\sim$ 12 K at 5 kbar, appearing when the low pressure transition is suppressed sufficiently but before the resistivity is reduced dramatically by the high pressure transition. As such, they have concluded that the superconductivity exist only when there are sufficient magnetic excitations to allow for Cooper pair formation. If these fluctuations are fully removed, superconductivity does not persist.

Pressure-induced superconductivity in $CaFe_2As_2$ was observed initially for applied pressures between roughly 0.25 and 0.9 GPa using liquid clamp-cell pressure measurements on Sn- flux solution-grown $CaFe_2As_2$.[41, 40] This is in contrast with $BaFe_2As_2$ and $SrFe_2As_2$, which require pressures in the range from 2.8 to 6 GPa for the highest T_C $\sim$28 K.[42] The new phase has

a tetragonal structure but with a reduced c-lattice parameter, hence termed volume-collapsed tetragonal (cT).[6] Kreyssig *et. al* used a He gas pressure cell to study the phase transitions of $CaFe_2As_2$ as a function of pressure and temperature using x-ray and neutron diffraction.[6] At 50 K at ambient pressure, the neutron-diffraction scan through the nuclear $(2\ 2\ 0)_T$ diffraction peak showed a splitting into the orthorhombic $(4\ 0\ 0)_O$ and $(0\ 4\ 0)_O$ peaks, a clear signal of a orthorhombic phase as seen in the diffraction pattern (A), Figure 1.6(b). In the inset of the same figure, a magnetic peak at $(1\ 2\ 1)_O$ was also observed. These results are evidence of the low-temperature orthorhombic phase of a $CaFe_2As_2$ compound. The orthorhombic structure and antiferromagnetic phase remained up to pressure of 0.24 GPa. Above a pressure of 0.35 GPa, the magnetic peak disappeared and the orthorhombic structure was transformed into a tetragonal structure similar to the high-temperature tetragonal phase (Figure 1.3) but with a 5 % reduced volume. This non-magnetic phase has a c-lattice parameter reduced by ∼9.5% while the a-lattice parameter increases by ∼2%. The transition to the cT phase can be seen in the shift of the $(0\ 0\ 2)_T$ and $(2\ 2\ 0)_T$ nuclear peaks in Figure 1.6 [Diffraction pattern (B) for panels (a) and (b)].

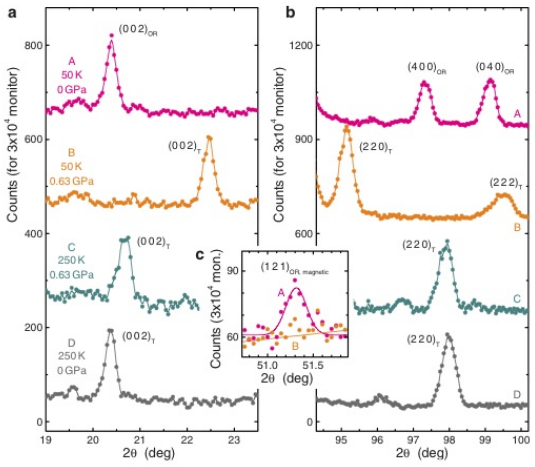

Figure 1.6 Neutron-diffraction pattern reproduced from reference [6]. The nuclear peaks are seen in (a) and (b). The peaks position changed as a result of significant changes in the lattice parameter. The magnetic $(1\ 2\ 1)_O$ diffraction peak is shown in (c).

Pressure-induced superconductivity in $CaFe_2As_2$ was said to emerge from a new phase formed under pressure rather than the magnetically ordered, low-temperature orthorhombic

phase or the high-temperature tetragonal phase. However, the experimental conditions for the pressure-dependent superconductivity are complicated and non-trivial with reports of sensitivity to the non-hydrostatic component of pressure. The measurements with hydrostatic pressure showed no evidence of superconductivity for P $<$ 0.6 GPa. This implies that the superconductivity arises from non-hydrostatic conditions from the pressure cell.[43] The study using hydrostatic pressure by W. Yu *et. al* also fail to observe the collapsed tetragonal phase. The cT phase is not unique to parent $CaFe_2As_2$ under pressure but also has been realized under isovalent (P) doping and electron (Rh) doping.[44, 45] Studies have confirmed that superconductivity disappears in all the cT phase of $CaFe_2As_2$, manifested by isovalent (P) doping, electron (Rh) doping, and hydrostatic pressure. However, the substitution of Ca by Sr suggested that superconductivity does exist in the cT phase with $T_C \sim 22$ K.[46] Superconductivity with T_C of up to 49 K was also observed for the partial substitution of Ca by selected rare-earths (R = La, Ce, Pr, Nd).[47] Superconductivity was simultaneously observed by Saha et al. (T_C = 47 K in $Ca_{1-x}Pr_xFe_2As_2$ [48]), Gao *et al.* (T_C = 42.7 K in $Ca_{1-x}La_xFe_2As_2$ [49]), and Lv *et al.* (T_C = 49 K in $Ca_{1-x}Pr_xFe_2As_2$ [39]). Co-doping by La and P ($Ca_{1-x}La_xFe_2(As_{1-y}P_y)_2$) also induces superconductivity, with T_C of 45 K.[50]

These studies proposed that the superconducting phase exist in the non-magnetic cT phase, void of spin fluctuations. This contradicts with the theory of spin fluctuation pairing mechanism.[46, 48] Due to the mixed reports, many research has been performed to understand the nature of the phase, whether the phase is truly non-superconducting, and whether the phase is non-magnetic, supporting the idea of magnetic-fluctuation-mediated superconductivity rather than the traditional phonon pairing. Since a dramatic collapse of lattice parameter is seen in the *c*-axis, uniaxial pressure was applied along the *c*-axis of $CaFe_2As_2$ single crystals by Prokes *et. al.*[51] They found that superconductivity in the original liquid clamp-cell measurements non-hydrostatic component stabilizes the tetragonal phase down to 1.7 K for 0.075 $<$ P $<$ 0.3 GPa.

Magnetic fluctuations as pairing mechanism

The co-existence and competition of the phases have intrigued scientist to study the superconducting state with more detail. An inelastic neutron scattering study of the potassium-doped Ba122 demonstrated the existence of a resonant magnetic excitation in the superconducting phase at an energy transfer of about 14 meV and a momentum transfer of 1.15 Å.[52] The inelastic neutron scattering intensity as a function of momentum transfer, **Q**, and energy transfer is shown in Figure 1.7 (a) and (b). The value of **Q** corresponds to the antiferromagnetic wave-vector observed in the undoped parent compound, $BaFe_2As_2$. In Figure 1.7(c), the integrated intensity over (**Q**, ω) around the magnetic excitation shows the development of magnetic excitation below T_C. As such, the remaining AFM spin fluctuations have been proposed to be a possible Cooper pairing mechanism in iron-pnictide superconductors, an alternative to the phonon pairing mechanism. This pairing mechanism has been suggested because of a general trend that superconductivity appears in close proximity to the antiferromagnetic ordering. The close proximity indicates that the correlated antiferromagnetic fluctuations in these compounds play a crucial role in high-temperature superconductivity of iron-pnictides.[4, 1, 53] First-principle calculations of electron-phonon coupling also have concluded that conventional BCS superconductivity cannot account for high T_C and there must be other pairing mechanism in iron-pnictide superconductors.[4] Hence, one of the main concerns in studying iron-pnictide superconductors is to understand the relationship between the magnetism and superconductivity, particularly the role of spin dynamics in $CaFe_2As_2$.

The collapsed phase appears to be non-magnetic. The elastic neutron-scattering experiments conducted on $CaFe_2As_2$ found that the static magnetic ordering disappears in the collapsed tetragonal phase [33] and the spin-polarized total-energy calculation on the collapsed phase showed a reduced Fe moment.[6] In that study, using a local-density approximation, it was found that the tetragonal phase is lowest in total energy for a 5% volume reduction. The quenched magnetic-moment ground state is consistent with experimental observations of the loss of magnetic order in the cT phase and the strong decrease in resistivity observed upon crossing the boundary from the T to cT phases.

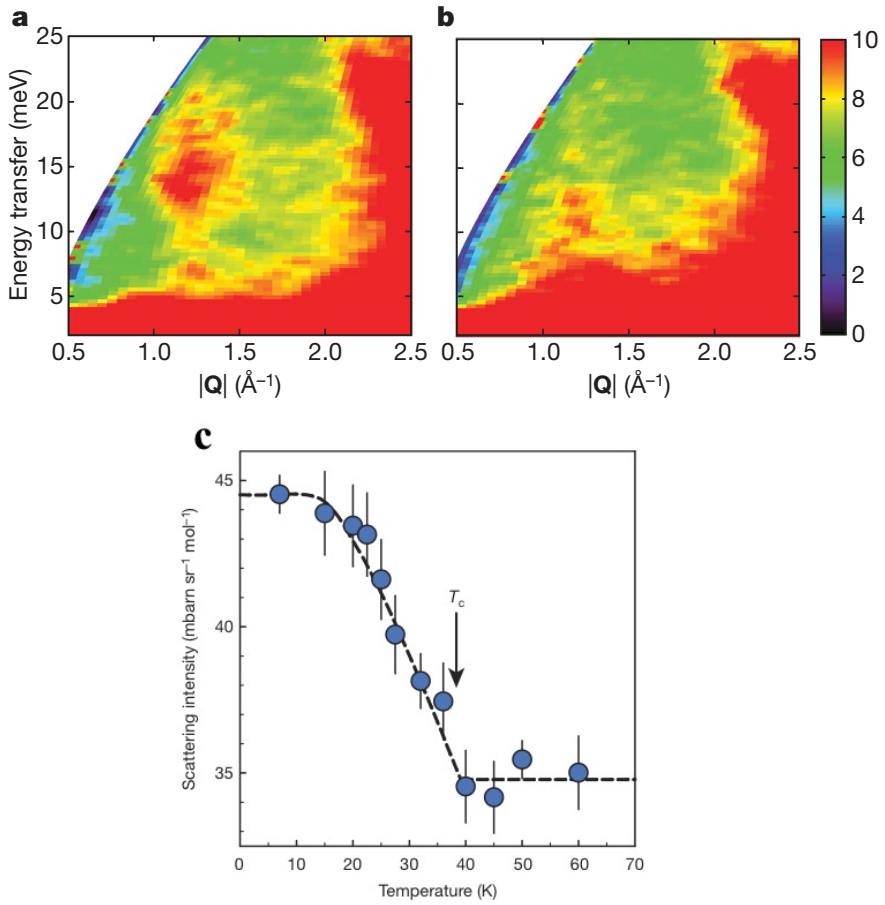

Figure 1.7 Inelastic neutron scatting intensity as a function of energy transfer (meV) and momentum transfer, **Q** for $Ba_{0.6}K_{0.4}Fe_2As_2$ at temperatures below (a) and above (b) superconducting temperature. (c) The integrated intensity over **Q** in the range 1.0 - 1.3 $Å^{-1}$ shows magnetic excitation below T_C.

In addition to the disappearance of magnetic ordering, neutron scattering measurements on the system showed that the collapsed phase does not appear to have spin fluctuations at low energies. Neutron scattering performed on $CaFe_2As_2$ has shown 2D paramagnetic spin fluctuations that persist up to 300 K ($1.8 \times T_N$).[54] While strong but short-ranged antiferromagnetic (AFM) correlation spin fluctuations have been found in the tetragonal phase, inelastic neutron scattering measurements showed that the fluctuations seemingly disappear in the collapsed tetragonal phase and, as mentioned previously, under hydrostatic pressure conditions the collapsed phase in $CaFe_2As_2$ does not support bulk superconductivity.[7] Pratt and co-workers performed measurements under hydrostatic pressured region and showed that the collapsed

tetragonal phase is characterized by the strong suppression *or* absence of the antiferromagnetic spin fluctuations observed in the ambient pressure, paramagnetic tetragonal phase (see Figure 1.8). The suppression, however, was only shown for a small momentum and energy space, thus leaving possibilities that the low-energy spin fluctuations are re-distributed elsewhere.

In summary, strong but short-ranged (AFM) correlated spin fluctuation have been found in the tetragonal phase, but their strong suppression or absence in the cT phase that does not undergo superconductivity makes it fascinating to study $CaFe_2As_2$. One thing to note is that the suppression of long-range magnetic ordering does not necessarily lead to the absence of spin fluctuations.

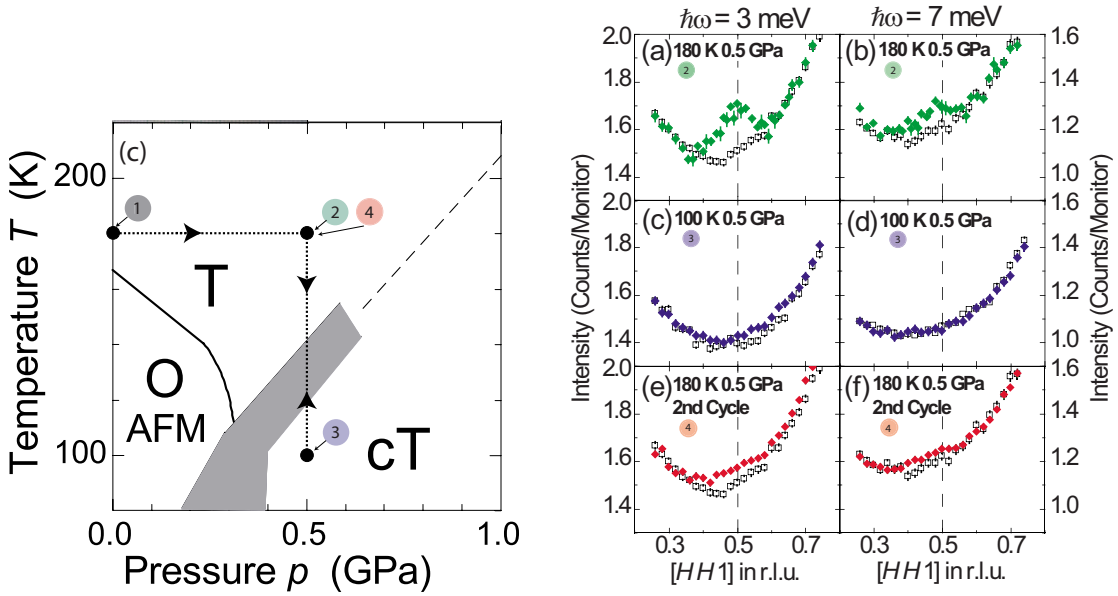

Figure 1.8 (Left) The temperature (K) versus pressure (GPa) phase diagram of $CaFe_2As_2$ from reference [7]. The sequence of experiments is labeled with color coded 1,2,3,4. The spin fluctuations of each steps can be seen on the right. (Right) Magnetic excitation can be seen at high temperature with pressure of 0.5 GPa. The magnetic excitation is clearly suppressed at 100 K. When the experiment is repeated at 180 K and 0.5 GPa, the magnetic excitation is there but at with a lower signal due to the impact from the T-cT transition causing the dislocation of single crystals.

1.4 Motivation and Organization of this Thesis

In the two families of high-temperature superconductors, cuprates and iron-pnictides, superconductivity emerges in close proximity to an antiferromagnetically ordered state.[55, 20, 56] As such, many consider magnetic fluctuations to be important. The disappearance of magnetic ordering and the proposed absence of spin fluctuations in this volume "collapsed tetragonal" (cT) phase of $CaFe_2As_2$ makes it an interesting compound to study. In our FeAs flux-grown $CaFe_2As_2$ material, the sample enters a collapsed tetragonal phase merely by tuning the temperature parameter. This is in contrast with previous Sn-grown samples, which required the use of a pressure cell. The experimental conditions for pressure-dependent superconductivity are complicated because of the sensitivity to the non-hydrostatic component of pressure. Hence, the ability to induce the collapsed tetragonal state with temperature will allow us to study accurately the state without the influence of pressure cells. This also allows for studying of the sample at a wider range in momentum and energy transfer to see if the antiferromagnetic (AFM) fluctuations are truly suppressed in the collapsed-tetragonal phase. The spin fluctuations of $CaFe_2As_2$ were studied at the high-temperature tetragonal (T) phase and low-temperature, cT phase using Inelastic Neutron Scattering (INS). Time-of-flight measurements were carried out using the Wide Angular-Range Chopper Spectrometer (ARCS) at the Spallation Neutron Source, Oak Ridge National Laboratory (ORNL). As this thesis is concerned with inelastic neutron scattering measurements of magnetic excitations $CaFe_2As_2$, the scattering theory, theoretical models and experimental techniques are presented in Chapter 2. The results and summary are reported in chapter 3.

CHAPTER 2. INELASTIC NEUTRON SCATTERING

2.1 Introduction

Neutron scattering techniques are used to study both static crystal and magnetic structures, and the dynamics of condensed matter systems. The basic characteristics of neutrons as well as the availability of high-flux neutron sources and instrumentation, like time-of-flight and triple-axis instruments, make neutron scattering the technique of choice to probe the dynamics of materials. Neutrons do not have electric charge. As a result, they experience weak or no Coulomb interactions with charged particles, and hence penetrate deeply into materials to interact with the nuclei. Although charge-less, the neutron has spin (s=1/2) and a magnetic moment that is able to interact with the unpaired electrons. As a result, they are a good probe of magnetic systems and of the excitations of such systems in materials. The mass of the neutron is 1.675 x 10^{-27} kg, leading to a thermal-neutron de Broglie wavelength ($\lambda = h/mv$) of about ~1.8 Å. This wavelength is of the order of the interatomic distances, making interference patterns possible and giving structural information about the condensed matter. In addition, thermal and cold neutrons have energies from 0.1 meV to 100 meV, comparable with thermal energies k_BT at room temperature and also elementary excitations in matter. As such, thermal neutron energies can be used to study low-energy excitations in the condensed matter such as lattice dynamics and magnetic excitations. X-rays with wavelengths of that order have energies in the kilo-electron-volt range. A summary of the basic properties of neutrons is given in Table 2.1. This chapter will outline the required technique and analysis in an inelastic neutron scattering experiment. The required ingredients of the experiments include: the source of neutrons, a method to prescribe or determine the incident and scattered wavevector, a well-chosen sample, a detector and the description of the scattering function.

Properties	**neutron**
mass	1.675 x 10^{-27} kg
charge	0
spin	$\frac{1}{2}$
magnetic dipole moment	$\mu_n = \frac{-e\hbar}{2m_n} g_n s_n$
energy	$E = \frac{\hbar^2 k^2}{2m_n}$ $k = \frac{2\pi}{\lambda}$
	$E(meV) = \frac{81.81}{\lambda^2[\mathring{A}]}$

Table 2.1 Basic properties of the neutron and electron.

2.2 Neutron sources

Neutrons for scattering measurements are produced using one of two general mechanisms: a) fission in a nuclear reactor; and b) spallation processes from bombarding heavy metal atoms with energetic protons from accelerators. Nuclear fission processes in reactors provide a continuous flux ($\sim 10^{15}$ n/cm^{2}s) while spallation processes provide pulses of neutrons up to $\sim 10^{17}$ n/cm^{2}s peak flux. The neutrons generated from the two sources have very high energies and thus are moderated to have useful energy ranges (cold, thermal, or hot depending on the temperature/energy range).

Pulsed sources produce short, strong bursts of neutrons as heat is deposited in the target only during the pulses. This allows for heat to dissipate slowly and continuously between pulses, allowing for very high instantaneous power and neutron flux.[57] This has its advantage over traditional, steady-state, high-flux reactors since less heat is dissipated in a spallation source than a fission process in a nuclear reactor producing the same time-average neutron flux. The experiment in this thesis was conducted using a pulsed source at the Spallation Neutron Source (SNS) at Oak Ridge National Laboratory (ORNL), TN. At a maximum beam power, it is one of the most intense neutron sources available, providing excellent statistical sensitivity. The current SNS power allows for high neutron flux so that small samples can be studied in detail. This is significant, as single crystals are difficult to grow and therefore are usually not big enough for very small effects to be measured.

2.3 Neutron scattering Theory

Neutrons are scattered by nuclei (nuclear scattering) and by the unpaired electrons of the magnetic atoms (magnetic scattering). The principle of the magnetic neutron scattering technique is covered in detail in many books.[58, 59, 60] In a scattering experiment, a source creates an incident beam that is scattered through its interaction with a sample. The final energy spectrum is measured by a detector as a function of scattering angle. By analyzing the differences between the incident and final beam energies, we can obtain important static and dynamic information about materials. If we define the incident beam by its wave vector $\boldsymbol{k_i}$ and its energy E_i (See Figure 2.1), after scattering by a sample, the wave vector and energy are $\boldsymbol{k_f}$ and E_f. The angle between the incident and final beams is 2θ. For any scattering experiment, the momentum ($\hbar\mathbf{Q}$) and energy($\hbar\omega$) change are obtained from the conservation laws of momentum and energy:

$$\mathbf{Q} = \mathbf{k}_i - \mathbf{k}_f \tag{2.1}$$

$$\hbar\omega = E_i - E_f \tag{2.2}$$

The *scattering vector*, $\mathbf{Q}$, often referred to as momentum transfer, forms the scattering triangle with $\boldsymbol{k_i}$, and $\boldsymbol{k_f}$ as shown in Figure 2.1. Here, the sign convention for $\mathbf{Q}$ is according to Lovesey (1984), differing from Bacon (1975), where $\mathbf{Q}$= $\mathbf{k}_f$ - $\mathbf{k}_i$.[59] In an experiment, we measure the number of scattered neutrons as a function of $\mathbf{Q}$ and ω.

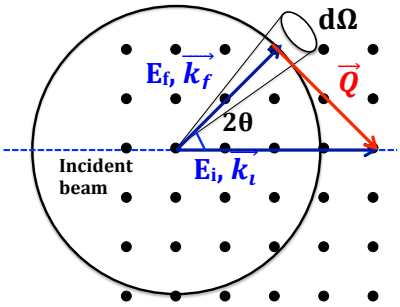

Figure 2.1 Incident neutrons with specific wavevector $\boldsymbol{k_i}$ and E_i are scattered by the sample into a final state $\boldsymbol{k_f}$ and E_f. Here, the geometry of the inelastic neutron scattering process for energy loss ($\boldsymbol{k_f} < \boldsymbol{k_i}$) is shown. For energy gain, $\boldsymbol{k_f} > \boldsymbol{k_i}$. The solid angle subtended by the detector is denoted as $d\Omega$.

For neutrons scattered through an angle of 2θ, the magnitude of the momentum transferred is

$$|\mathbf{Q}|^2 = k_{\mathbf{i}}^2 + k_f^2 - 2k_i k_f cos2\theta \tag{2.3}$$

Given the dispersion relation of the neutron $E = \frac{\hbar^2 k^2}{2m_n}$, the energy conservation equation can be written as:

$$\Delta E = \hbar\omega = \frac{\hbar^2}{2m_n}(k_i^2 - k_f^2) \tag{2.4}$$

The magnitude of the wave vector is $k = 2\pi/\lambda$, where λ is the wavelength of the neutron beam. For elastic scattering, $\mid \mathbf{k}_i \mid = \mid \mathbf{k}_f \mid = k$ and the energy transfer is zero. For inelastic scattering, $\mathbf{k}_i \neq \mathbf{k}_f$ due to the energy gain or loss of the neutron when scattered by the sample. This gain or loss is due to the annihilation or creation of excitations in the sample. The energy change is measured to gain information about dynamics of the material.

2.3.1 Neutron scattering cross section

In an experiment, the incident neutron flux, Φ, is the number of neutrons per second going through a unit area perpendicular to the direction of the beam at sample position. The quantity measured in neutron scattering experiments is the double differential scattering cross section which is the number of neutrons scattered into solid angle $d\Omega$ per second with energy in the range of E to $E + dE$, normalized to the incident flux, i.e

$$\frac{d^2\sigma}{d\Omega dE} = \frac{\begin{array}{c}\#\text{ neutrons scattered into solid angle } d\Omega \text{ per second} \\ \text{around } \Omega(\theta,\phi) \text{ with final energy between } E \text{ and } E+dE\end{array}}{\Phi d\Omega dE} \tag{2.5}$$

The double differential cross section is the sum of a coherent and an incoherent term. The coherent part gives information about the scattering due to the collective effects among different atoms, such as elastic Bragg scattering or scattering by lattice vibrations (phonons) and spin excitations (magnons). The incoherent scattering is the scattering from an individual atom, without any interference effects. It shows the time correlations of an atom with itself, giving

information such as the particle's motion. The coherent term is the only term of interest for spatial correlation. The differential cross section is the counting rate in $d\Omega$ for all energies is

$$\frac{d\sigma}{d\Omega} = \int_0^\infty \frac{d^2\sigma}{d\Omega dE}\, dE \tag{2.6}$$

and the total scattering cross section is

$$\sigma_{total} = \int_{all\ direction} \frac{d\sigma}{d\Omega}\, d\Omega. \tag{2.7}$$

The scattering cross section is measured in barns (1 barn = 10^{-28} m^2), which is a relatively weak interaction. As such, neutron scattering can be modeled using first-order perturbation theory. Scattering due to nuclei has a strong force but the potential is short-range and only s-wave (l=0) scattering is possible. For magnetic scattering, the potential is not short-range but is weak. Consequently, Fermi's golden rule for first-order perturbation can be applied to calculate the probability of transitions, and in the scattering process is equivalent to the Born approximation. For neutrons scattered by an interaction potential, V, of the neutron-sample system, the neutrons will undergo a change of state from ($\boldsymbol{k_i}$,σ_i) to ($\boldsymbol{k_f}$,σ_f) while the sample changes from λ_i to state λ_f. The double differential cross section is then given as

$$\frac{d^2\sigma}{d\Omega\, dE}_{k_i \to k_f} = \frac{k_f}{k_i}\left(\frac{m}{2\pi\hbar^2}\right)^2 \mid \langle k_f \sigma_f \lambda_f \mid V \mid k_i \sigma_i \lambda_i \rangle \mid^2 \delta(E_{\lambda_i} - E_{\lambda_f} + E_i - E_f) \tag{2.8}$$

with E_i-E_f= $\hbar w$. Using the Born approximation and treating the incoming and outgoing neutrons as plane waves, the potential interaction matrix elements can be calculated. V is the Fourier transform of the potential function for the neutron-sample interaction potential

$$V(Q) = \int d\mathbf{r}\ V(\mathbf{r}) e^{i\mathbf{Q}.\mathbf{r}} \tag{2.9}$$

Magnetic interaction potential

Magnetic scattering of neutrons is due to the interaction of the magnetic dipole moment of the neutron ($\boldsymbol{\mu_n}$=-$\gamma\mu_N\boldsymbol{\sigma}$) with the magnetic field produced by the unpaired electrons (momentum $\mathbf{p}$, spin $\mathbf{s}$ and dipole moment $\boldsymbol{\mu_e}$=-$2\mu_B\boldsymbol{s}$) in a magnetic material. The value of γ is

1.9132 while μ_N and μ_B are the nuclear and Bohr magneton respectively. The magnetic field is determined by the total magnetization from the magnetic moments due to the spin and orbital motions. For nuclear scattering of unpolarized neutrons, the double differential cross section does not depends on the spin state. The magnetic potential V_m, however, needs to specify both the wave vector k and the spin state of the neutron. The magnetic interaction potential of a neutron with the sample's magnetic field $B(r)$ as a function of both the intrinsic spin and the orbital motion of the electrons can be written as

$$V_m(r) = -\mu_n \,.\, \mathbf{B}(\mathbf{r}) = -\,\mu_n \,.\, (\mathbf{B_s} + \mathbf{B_l}) = \frac{\mu_0}{4\pi}\,[\,\nabla \times (\frac{\mu_\mathbf{e} \times \hat{\mathbf{R}}}{R^2}) - \frac{2\mu_B}{\hbar}\frac{\mathbf{p} \times \hat{\mathbf{R}}}{R^2}] \quad (2.10)$$

The magnetic scattering cross section that takes the neutron spin state from, σ_i to ,σ_f and the scattering system from λ_i to λ_f is

$$\frac{d^2\sigma}{d\Omega\, dE}_{\sigma_i\lambda_i \to \sigma_f\lambda_f} = (\frac{\gamma r_0}{2\mu_B})^2 \frac{k_f}{k_i} \mid \langle \sigma_f\lambda_f \mid \sigma.\mathbf{M}_\perp \mid \sigma_i\lambda_i \rangle \mid^2 \delta(E_{\lambda_i} - E_{\lambda_f} + \hbar\omega) \quad (2.11)$$

where $\mathbf{M}_\perp(\mathbf{Q})$ is the component of the Fourier transform of the magnetization that is perpendicular to the scattering vector $\mathbf{Q}$.

2.3.2 Dynamical structure factor, $S(\mathbf{Q}, \omega)$

Using the methods shown by Van Hove (1954) and described in standard text books, the double differential cross section can be expressed as proportional to the dynamical structure factor S($\mathbf{Q}$,ω), [59]

$$\frac{d^2\sigma}{d\Omega\, dE} = N\frac{k_f}{k_i} S(\mathbf{Q}, \omega) \quad (2.12)$$

where

$$S(Q, w) = \frac{1}{2\pi\hbar N} \sum_{ll'} \int_{-\infty}^{\infty} dt\ \langle e^{-i\mathbf{Q}.\mathbf{r}_{l'}(0)} e^{i\mathbf{Q}.\mathbf{r}_l(t)} \rangle\ e^{-iwt} \quad (2.13)$$

N is the number of nuclei, t is the time. This allows us to separate k_f/k_i, the experimental setup-dependent term, from $S(\mathbf{Q}, w)$, the sample-only dependent term. The term in the sum,

$\langle e^{-i\mathbf{Q}.\mathbf{r}_{l'}(0)} e^{i\mathbf{Q}.\mathbf{r}_l(t)} \rangle$, represents the correlation between the position of one nucleus at time t = 0 with another nucleus at a time t later. As such, $S(\mathbf{Q}, w)$ also referred to as dynamical correlation function, gives the microscopic properties of the condensed matter, measuring the strength of the correlations or the collective effect.

Neutron scattering directly measures the scattering function, $S(\mathbf{Q}, \omega)$. As mentioned, the scattering function can be separated to two parts: (i) the elastic scattering resulting from static order of magnetic moments in a system and (ii) inelastic magnetic scattering from their motion. The the elastic term is a delta-function in energy, the scattering usually dominates at zero energy transfer. If there is no elastic contributions such as Bragg scattering, then $S(\mathbf{Q}, \omega)$ corresponds to the fluctuations in a sample. Another process, quasi-elastic scattering, also peaks at zero energy transfer but is broadened compared to the elastic function due to diffusive processes. Both quasi-elastic scattering and elastic scattering may co-exist. A comparison of the elastic, quasi-elastic and inelastic scattering function can be seen in Figure 2.2.

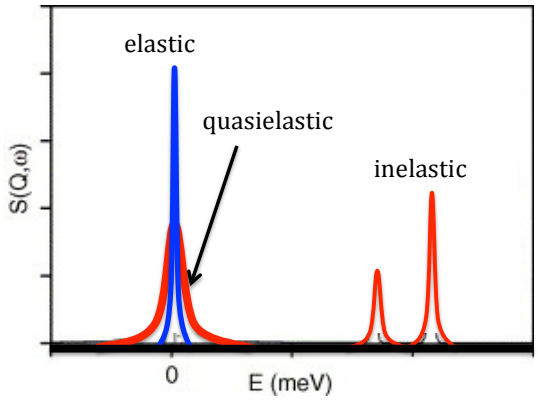

Figure 2.2 Schematic representation of quasi-elastic and inelastic scattering function, $S(Q, \omega)$ as a function of energy transfer at a constant Q. The dotted line is the elastic scattering function. Energy gain (loss) causes the inelastic function to peak at negative (positive) energy transfer.[8]

As this experiment centers around the inelastic neutron scattering of the magnetic system, specifically the spin excitation of $CaFe_2As_2$, the discussion will focus on inelastic magnetic scattering. The dipole approximation for the spin-only double differential cross section in magnetic inelastic neutron scattering measurements is given as:

$$(\frac{d^2\sigma}{d\Omega dE})_{mag,in} = \frac{k_f}{k_i}(\frac{\gamma r_0}{2})^2 f^2(Q) e^{-W(\mathbf{Q},T)} S(\mathbf{Q},w) \tag{2.14}$$

for magnetic form factor $f^2(Q)$ and the temperature-dependent Debye-Waller factor $e^{-W(\mathbf{Q},T)}$ from small fluctuations of the position of magnetic ions. The magnetic scattering cross section is only due to the component of the neutron spin that is perpendicular to the momentum transfer, $\mathbf{Q}$. In this thesis, we use the iron Fe^{2+} magnetic form factor ($< j_0 >^2$ in Figure 2.3) because the sample is a Ca-based iron-arsenide superconductor. The magnetic form factors falls off rapidly as a function of Q.

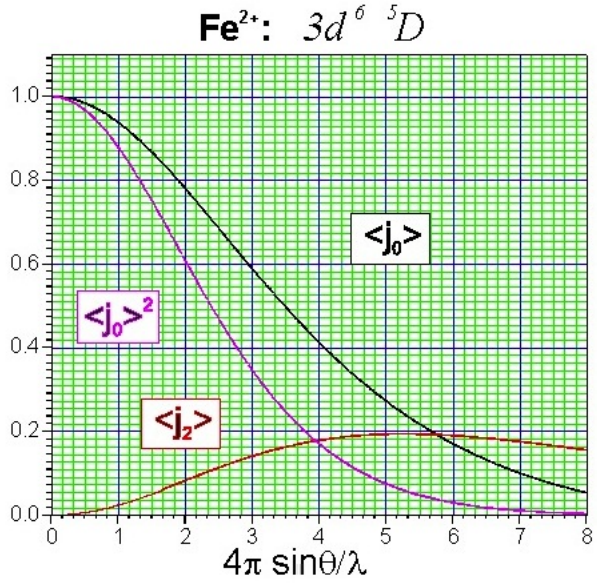

Figure 2.3 Iron Fe^{2+} magnetic form factor.

There are two important properties of the dynamical correlation function, one of which is the principle of detailed balance,

$$S(-\mathbf{Q},-\omega) = e^{-\hbar\omega/k_B T} S(\mathbf{Q},\omega) \tag{2.15}$$

where k_B is the Boltzmann's constant, T is temperature and ω is positive. The principle of detailed balance shows that the probability of a transition will be $e^{-\hbar\omega/k_B T}$ lower for excitation due to annihilation than for excitation due to creation. In other words, it is more probable that the system is in ground state, and takes the energy from the neutron than being in the excited state, giving energy to the neutron. The second property, the fluctuation-dissipation theo-

rem, gives the proportionality to χ"$(\mathbf{Q},\omega)$, the imaginary part of the dynamical susceptibility through

$$S(\mathbf{Q},\omega) = \frac{\chi''(\mathbf{Q},\omega)}{\pi(1-e^{-\hbar\omega/k_BT})}, \tag{2.16}$$

The Bose thermal factor is given as $(1-e^{-\hbar\omega/k_BT})$. Note: Boltzmann's constant, k_B, is 1.381×10^{-23} Joules/K and so $\hbar/k_B = 11.60$ K/meV. The dynamical magnetic susceptibility, $\chi(\mathbf{Q},\omega)$, measures the system's response to magnetic field and the imaginary part of it, $\chi''(\mathbf{Q},\omega)$, measures the energy dissipated by the system. The fluctuation-dissipation theorem is used to compare the magnetic scattering measurements to theoretical models of $\chi''(\mathbf{Q},\omega)$ that are available. In the next section, a brief discussion of the theoretical model χ"$(\mathbf{Q},\omega)$ in reference [54] by S. Diallo *et. al* will be presented.

2.3.3 Magnetic excitations

In magnetic materials, ordered spins can be disrupted by spin waves, and these energies are quantized as magnons similar to the thermally excited lattice-vibration disruptions in a crystal lattice, phonons. As with phonons, magnons are described by a dispersion relationship between the energy and wave vector. The measurements of magnetic excitation are important in understanding the exchange interactions that are present in a system. Inelastic neutron scattering has been widely used to measure spin excitation spectra for the iron-pnictide superconductors especially the 122-family.[61, 62, 63, 64] For the iron arsenides, above T_N, a theoretical model of the paramagnetic spin excitations was developed by S. Diallo in reference [54], following several distinct features including diffusive spin for the energy range measured (<60 meV) and a two-dimensional excitation with a weak dependence along c. The magnetic susceptibility can be written as

$$\chi''(\mathbf{Q},\omega) = \frac{\hbar\omega\gamma\chi_0}{(\hbar\omega)^2+\gamma^2\{(q^2+\eta q_x q_y)a^2+(\frac{\xi_T}{a})^{-2}+\eta_c[1+cos(\pi L)]\}^2} \tag{2.17}$$

where χ_0 is staggered susceptibility, ξ_T is the magnetic correlation length at temperature T in units of Å, and γ is the damping coefficient from the spin decay into particle-hole excitations.

Γ_T is the Lorentzian energy width and $\gamma = \Gamma_T(\frac{\xi_T}{a})^2$. Here, $\mathbf{Q} = \mathbf{Q_{AFM}} + \mathbf{q}$ where $\mathbf{q}$ is the distance from the magnetic zone center and $q^2 = q_x^2 + q_y^2$. Two dimensionless parameters describe the anisotropy of the in-plane correlation lengths (η) and the strength of the interlayer spin correlations ($\eta_c = J_C\chi_0$). The in-plane anisotropy η can be obtained from the longitudinal (+) and transverse (-) correlation lengths,

$$\eta = 2\frac{\xi_{T+}^2 - \xi_{T-}^2}{\xi_{T+}^2 + \xi_{T-}^2} \tag{2.18}$$

The χ'' in equation 2.18 is not appropriate for ordered magnet as the spin wave concept is not useful in paramagnetic state. At $q = 0$ the model has a quasi-elastic response. The form used to describe diffusive excitation above T_N for $L = odd$, longitudinal scan is

$$\chi''(\mathbf{Q},\omega) = \frac{\hbar\omega\Gamma_T\chi_T}{(\hbar\omega)^2 + \Gamma_T^2(1 + q^2\xi_{T+}^2)^2} \tag{2.19}$$

Fitting done by S. O. Diallo resulted in as damping energy width of about 10 meV. The energy width depends on the decay time of the magnetization correlation function. As such, large damping describes short-range and short lifetime spin correlations. This model is used to describe the paramagnetic spin-fluctuations around the antiferromagnetic wave vector.

2.4 Instrumentation

There are several methods used in inelastic studies, including the triple-axis crystal spectrometer, the time-of-flight spectrometer and the neutron spin-echo spectrometer. While the triple-axis spectrometer can only examine one position at a time in the momentum and energy (Q,E) space, the time-of-flight spectrometer can examine a wide coverage in the (Q,E) space by having detector arrays. For each detector pixel, the time of arrival to the detector is directly related to the energy exchange between the sample and neutrons. Time-of-flight spectrometers, in combination with single crystal samples, allow for the characterization of the full magnetic energy spectrum. This inelastic neutron scattering experiment was performed at the wide angular-range chopper spectrometer (ARCS) at the Spallation Neutron Source (SNS), Oak Ridge National Lab (ORNL). Here, a brief description of the time-of-flight (TOF) technique and analysis will be given.

2.4.1 Time-of-flight chopper spectrometer

For a direct TOF spectrometer, the incident energy is specified by either a monochromator (Bragg diffraction principle) or a chopper system. The beam is scattered off the sample and final energy is determined by time-of-flight between the sample and detectors. ARCS is a direct TOF spectrometer where E_i is preselected using a chopper system. The time-of-flight spectrometer yields information about the energy transfer caused by the elementary excitations of the sample,

$$\hbar\omega = E_i - E_f \tag{2.20}$$

The distances between the source and sample (D_i) and the sample and the detector (D_f) are known, while the arrival time, t, of each scattered neutron at the detector is recorded. The final neutron energy can be calculated knowing the velocity, $v = D_f/t$.

$$\hbar\omega = E_i - \frac{1}{2}m(\frac{D_f}{t})^2 \tag{2.21}$$

In a neutron time-of-flight chopper spectrometer like ARCS, a polychromatic beam goes through a series of neutron choppers, creating pulses of monochromatic beam at the desired wavelength. This is in contrast with the use of single crystal monochromators to monochromate the beam. A schematic diagram of a TOF-chopper spectrometer is shown in figure 2.4.

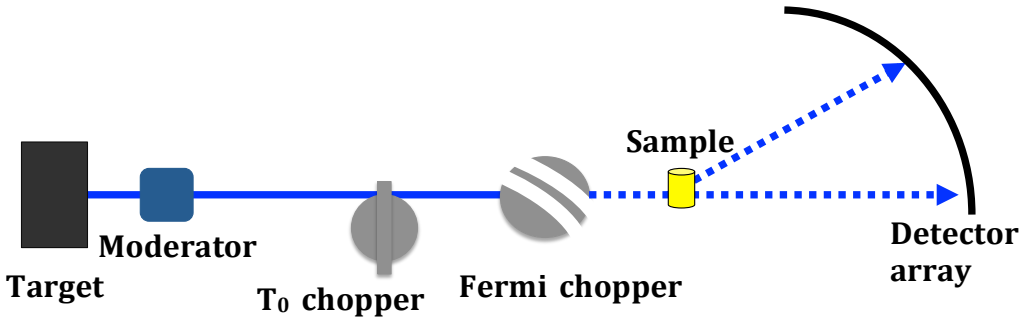

Figure 2.4 Schematic diagram of time-of-flight chopper spectrometer

Wide Angular-Range Chopper Spectrometer - ARCS

ARCS is optimized for high intensity neutron flux at the sample and has a large solid-angle of detector. The monochromatic neutron pulses created by the Fermi chopper scatter off the sample and are detected using an array of large solid angle detectors, as can be seen in Figure 2.5. ARCS uses an ambient temperature water moderator, and the incident energy range of 15 - 1500 meV (up to 5000 meV) can be selected to study a variety of excitations in condensed matter.[65]

Neutron choppers are rotating mechanical devices that block neutron for a fraction of the time during a rotation with the use of boron(neutron absorber) and aluminum (transparent to neutrons). ARCS has a series of choppers, principally a T_0 chopper and two Fermi choppers, as shown in the schematic in Figure 2.4. T_0 choppers have a large mass of high-cross-section material in the beam in order to block fast neutrons that are created immediately after the proton hits the target. T_0 choppers also rotate rapidly to allow the desired wavelength pulses to pass through. Fermi choppers are bandwidth limiting choppers that have a series of parallel slits spaced d apart that are rotated around an axis perpendicular to the beam at a frequency ν. The choppers rotate in some multiple or submultiple of the source frequency and are kept in phase with the source. This in-phase relationship is especially important for Fermi choppers. The resolution of the experiment is determined by slit width, rotation speed, moderator pulse width and lengths of instruments sections.[66]

A pulse of incident neutrons spreads out in time as it travels, and the fastest (highest energy) neutrons reach the chopper first. As it rotates, the chopper allows through a section of the pulse containing neutrons with the desired energy; faster or slower neutrons are blocked by the absorbing strips. The energy range or width is determined by the phase and frequency of the chopper rotation. Neutron choppers are ideally made for pulsed spallation sources. While they can be used at a steady-flux reactor source, the beam must be chopped into pulses before reaching the Fermi chopper, thus not optimizing the steady-state neutron flux produced. As the Fermi choppers are on a translation stage, they can be replaced and removed from the beam. A white beam is created when no Fermi chopper is in the beam and the T_0 chopper is

made to be out-of-phase with respect to the neutron pulse. The broad energy range can be used for diffraction measurements to characterize sample co-alignment quality.[65]

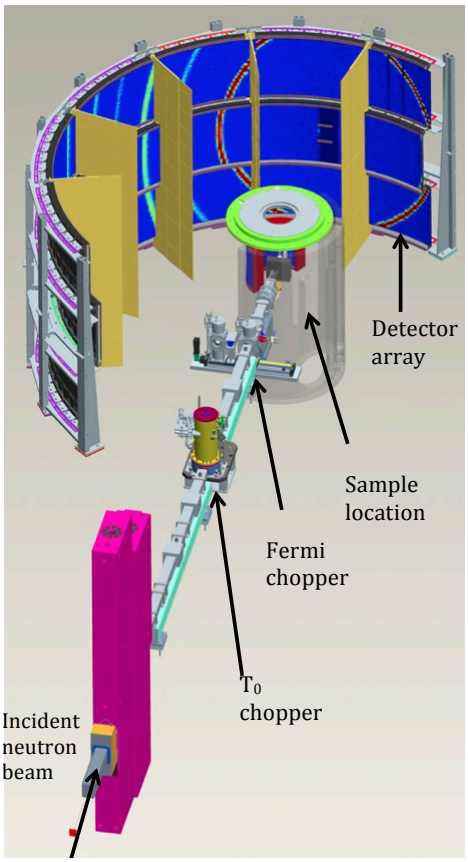

Figure 2.5 ARCS chopper spectrometer with a wide detector coverage. A powder diffraction pattern was superimposed on the detector.

The detector array consists of 115 modules or packs of eight 1-m long ^{3}He linear position sensitive detectors that are located in the vacuum scattering chamber, along with the electronics for optimal signal-to-noise ratio and space usage.[65] They operate within the vacuum with low power components and blackened surface to enhance radiative thermal transfer. A boron carbide based internal shielding using a special ZHIP (Zero Hydrogen in product shielding) mix was used.[65] This mix without hydrogen works for the high neutron energies and reduces the background noise while maintaining the performance in the vacuum chamber. The data from the detector are stored as a stream of neutron events, with information of the detector pixel and time-of-flight value when a neutron was detected. The events are correlated with the

proton pulse that generated the neutron source. The timestamp and proton charge information allows for the normalization of the incident beam using the proton charge. A large curved vertical translating gate valve separates the sample environment from the larger detector vacuum chamber. This avoids constant changes to the detector environment, and the vacuum in the sample chamber can be restored in under 15 minutes.[65]

ARCS Time-of-flight analysis

ARCS data records each scattered neutron's arrival time, t, at a detector's pixel at (ϕ, θ). Hence, the time-of-flight data need to be converted from the instrument coordinates $S_{\phi,\theta}(t)$ to spectra that are function of momentum and energy, $S(\mathbf{Q}, \omega)$. A standardized time-of-flight direct geometry spectrometer (dgs) reduction routine based upon functions within the Mantid software application was used.[67] The reduction routine was run from within a Python terminal at the ARCS station in SNS and was able to convert the independent time spectra from more than 60, 000 detector pixels into a distribution of energy and momentum transfer. The reduction process normalizes the data to total charge in Coulomb, and generates nxspe, phx, and spe data file types. These files can be visualized using DAVE-Mslice (http://www.ncnr.nist.gov/dave/), Mslice and a number of other programs. The reduced data is visualized and analyzed using both DAVE and Matlab-based Mslice software developed by Radu Coldea.[68] A few additional Matlab routines written by G.S. Tucker were also used.

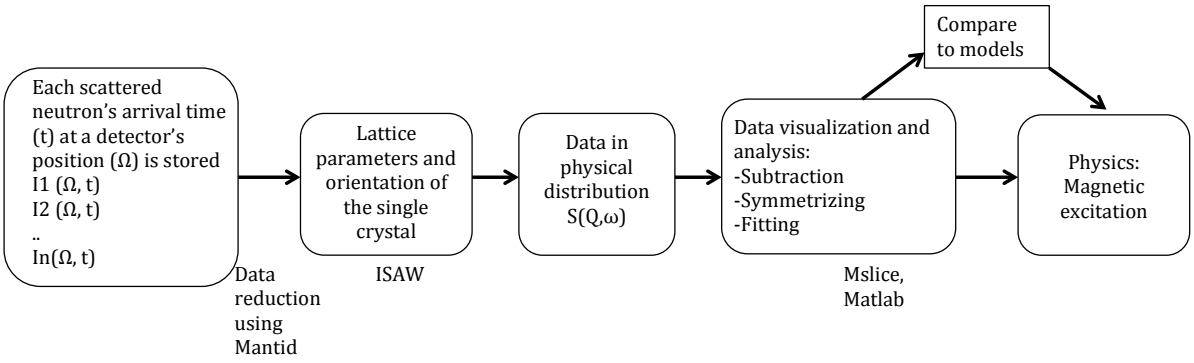

Figure 2.6 A flow diagram of the analysis

The co-aligned single-crystal sample quality was checked with a white beam for the orientation, and the crystal lattice was determined quickly using the Java ISAW software package at the station.[69] The software is able to take ARCS data in NeXus format [70] and calculate the Laue diffraction for a variety of peaks at a time, and the determined orientation was saved as a parameter file to be used by single-crystal inelastic-scattering visualization software Mslice.

The magnetic inelastic neutron scattering data is obtained by subtracting a background function $B(\mathbf{Q},\omega)$ from the measured intensity, $I(\mathbf{Q},\omega)$,

$$S(\mathbf{Q},\omega) = I(\mathbf{Q},\omega) - B(\mathbf{Q},\omega) \tag{2.22}$$

Various methods of background subtraction were done and compared. The usual practice is by subtracting a non-magnetic background estimated at a wave vector away from the peak at T = 150 K. The second which was performed in the current studies, is by subtracting the reduced data at T = 10 K (cT phase) from the data at T = 150 K (T phase) using **ms_minus.m** codes by G. S. Tucker. This subtracts the intensity in each detector-energy bin without any contributions due to rebinning and is likely more accurate background subtraction. Other methods included using a bose-factor corrected for low temperature data and masking of peaks at the antiferromagnetic wave vector (selecting an area around) before averaging around ϕ. The background was directly subtracted without any temperature factor as it was difficult to distinguish the scattering that is from from the samples or the sample holder. Given that the sample remains in the same holder the entire experiment, this was the best estimate of the background possible. The non-magnetic background was then used for studying of the spin fluctuations at high-temperature data.

The data is visualized with the following viewing axis u_1 = (1 1 0) and u_2 = (1 -1 0) with the peaks located in Figure 2.7. The low-temperature-background subtracted data was subsequently folded for symmetry equivalent to improve statistics using **ms_symgen** (modified by G.S. Tucker from T.G.Perring's Mslice codes). The data allow one to symmetrize the data in Mslice by reflecting through a plane chosen, not limited to the geometry in Mslice. In the analysis, whenever possible, the data was folded twice; (i) reflected through a plane across the diagonal and (ii) refolded into a quadrant.

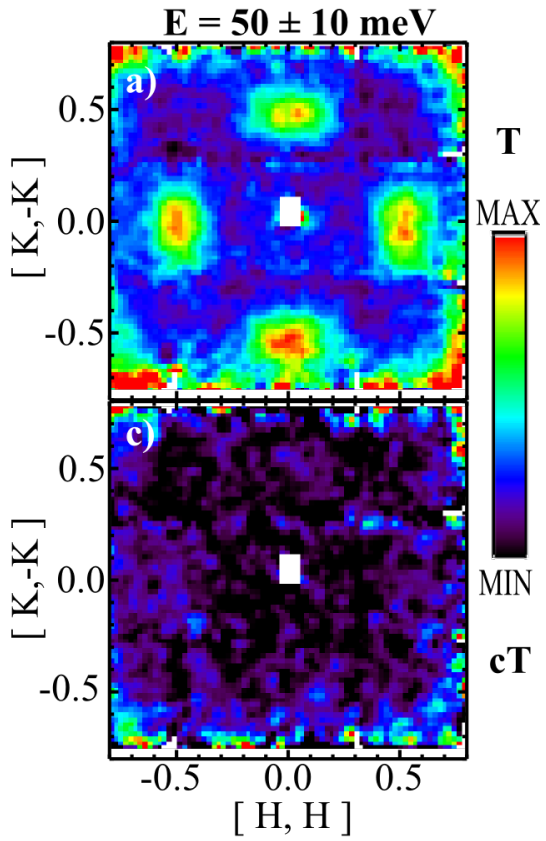

Figure 2.7 An example of a slice taken perpendicular to a constant energy transfer (**E = 50 ± 10 meV**) range projected with viewing axis u_1 = (1 1 0) and u_2 = (1 -1 0). The intensity of the scattered neutrons is given by the color bar in the figures. Black color indicates no scattered neutrons were detected while the white regions indicate no detection is possible with gaps in the detector coverage. Data were subsequently folded for symmetry equivalent across the diagonal as described in text.

Two-dimensional slices through the main crystallographic symmetry direction were performed in the H-K plane at different energies to visualize the magnetic excitations close to the antiferromagnetic wave vector as seen in Figure 2.7, and Figures 3.8 and 3.9 in Chapter 3. One-dimensional cuts (Figure 3.10, Chapter 3) through the magnetic fluctuations above the transition temperature were fitted in MATLAB to a 2D-spin fluctuations theoretical model by S. O. Diallo.[54] The energy dependence of a particular cut at an incident energy can also be obtained and fitted to the spin-fluctuation model as seen in Figure 3.10, Chapter 3.

CHAPTER 3. Experiment and Results

3.1 Experimental details

Inelastic neutron scattering (INS) was used to probe the magnetic excitations of $CaFe_2As_2$ in the tetragonal and collapsed tetragonal phase. The measurement was carried out using the Wide Angular-Range Chopper Spectrometer (ARCS) at the Spallation Neutron Source (SNS), Oak Ridge National Laboratory (ORNL). The outline for the technique and spectrometer is given in Chapter 3. Incident beam energies of $E_i = 75$ meV and $E_i = 250$ meV were selected for this experiment. INS data were collected for the high-temperature paramagnetic, tetragonal (T) phase at T = 150 K and the low temperature collapse tetragonal (cT) phase at T = 10 K. The sample was attached to the cold-finger of a cryostat and oriented with the tetragonal c-axis parallel to the incident beam, in order to easily describe the data using tetragonal $I4/mmm$ coordinate system.

3.1.1 FeAs-flux single-crystal growth and sample preparation

While initial characterization of most $CaFe_2As_2$ single crystals involved samples grown from Sn flux as described in reference [5], the single-crystal sample used in the present study was grown from ternary melts rich in FeAs by S. Ran.[9] The termed "as-grown" single crystals were grown from excess FeAs by rapidly cooling a ternary melt of $CaFe_4As_4$ from 1180 to 1020 °C over 3 hours, followed by slow cooling from 1020 to 960 °C over 35 hours, and then decanting off the excess liquid. The sample was then quenched from 960 °C to room temperature. Sn-grown single crystals are malleable, easily bent and deformed but the as-grown samples are brittle and shatter easily. Unlike Sn-flux grown crystals, FeAs flux grown crystals do not have well-formed facets, but the plates of the crystals are perpendicular to the crystallographic c-axis.

The typical dimensions for Sn grown samples are usually only several millimeters in length and with a thickness up to about 0.5 mm, but, in contrast, larger single crystals of $CaFe_2As_2$ have been grown from the ternary melt, $CaFe_4As_4$.[71, 9] The FeAs flux-grown sample enters a collapsed tetragonal phase at a lower temperature, and at ambient pressure. A comparison of the temperature-dependent magnetic susceptibility and normalized electrical resistivity of single crystals grown from various method are shown in Figure 3.1

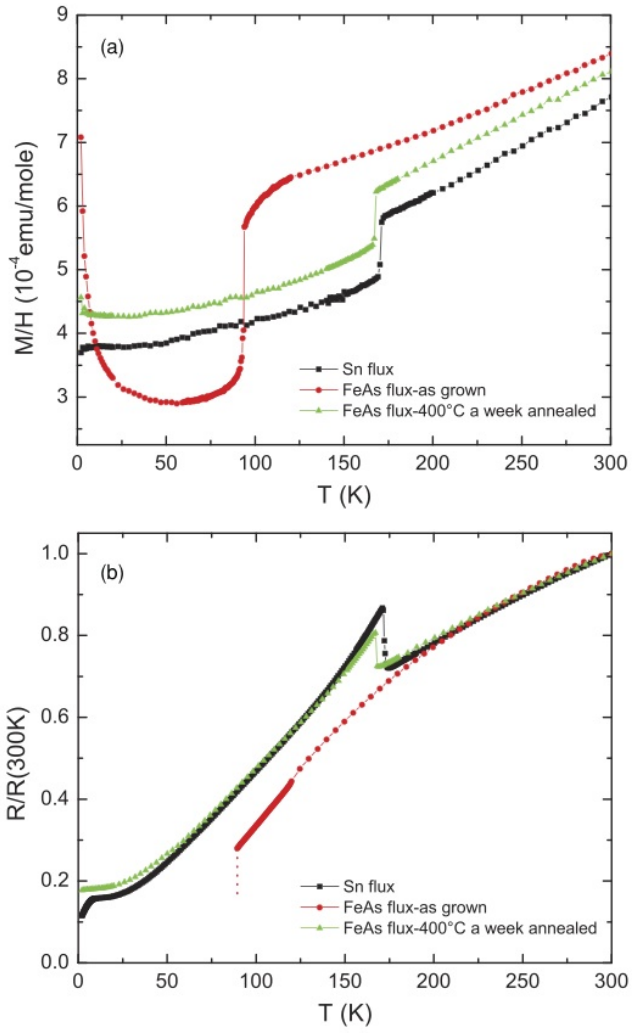

Figure 3.1 Temperature-dependent (a) magnetic susceptibility and (b) normalized electrical resistivity of $CaFe_2As_2$ for (i)Sn-grown (black squares) (ii) As-grown (quenched from 960 °C) from FeAs (red circles) and (iii) FeAs-grown, annealed for 1 week at 400 °C (green triangles). Lower-temperature resistivity measurements on as-grown sample were impossible because it shattered.[9]

The Sn-grown sample and FeAs grown sample that was annealed for 1 week at 400 °C showed similar behavior in resistivity and susceptibility. The increase in resistivity and decreases in susceptibility at 170 K is associated with the phase transition of $CaFe_2As_2$. As-grown sample (quenched from 960 °C), on the other hand, showed a very sharp decrease in magnetization slightly below 100 K. The strain field associated with a uniform distribution of fine-sized FeAs precipitates appears to play a key role in the ambient pressure transformation. Other than a shift in temperature, the transformation from the T phase to the cT phase at ambient pressure is consistent with the T-cT transformation observed for the Sn-flux solution-grown samples under applied pressure, eliminating the need for a pressure cell and, therefore, the size-able contribution it makes to the measured background in scattering measurements.

The co-alignment of 12 high quality single crystals provided a total mass of ≈1.5 g and the sample mosaic was 1.5° full-width-at-half-maximum. Each single crystals was chosen to have substantial mass of at least 90 mg and above. The biggest mass was $\sim$ 235 mg. The crystals were checked for sample quality – flat, smooth surface without layers, and if they are indeed single-crystals using Laue camera. The FeAs-grown plates do not have facets like the Sn-grown single crystals, they do conveniently have the *c*-axis perpendicular to the plates. Subsequently, they were aligned using Laue camera according to the tetragonal crystal structure (I4/mmm, space group =139) to form the large collection of co-aligned single crystals. See Laue pattern in Figure 3.2 The sample was oriented with (110) along the direction of the Al fingers and the tetragonal c-axis parallel to the incident beam. As neutrons scattered only weakly from aluminum, the single crystal sample was affixed on aluminum fingers with aluminum wire and aluminum foils as seen in Figure 3.3. The use of it was minimized to avoid excessive scattering by non-sample contributing to the background scattering. The scattering by Al phonons can be observed in the results at energy transfers less than $\sim$ 40 meV. The crystals were arranged such that they were concentrated to the center of mass of the entire sample, alternating between two and three crystals per plate. Neutron absorbing boron nitride shielding was added to the front of the sample at the lower side to reduce scattering due to the holders.

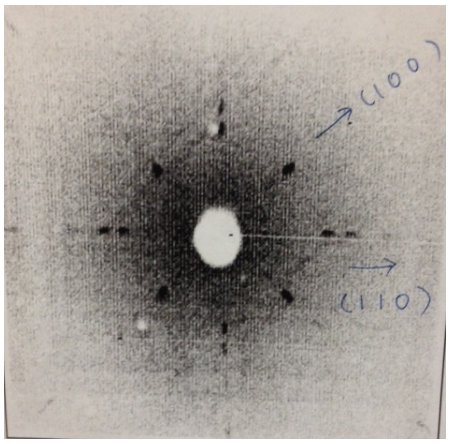

Figure 3.2 The Laue diffraction patterns for $CaFe_2As_2$ single crystals. The (110) direction is aligned along the direction of the fingers as seen below.

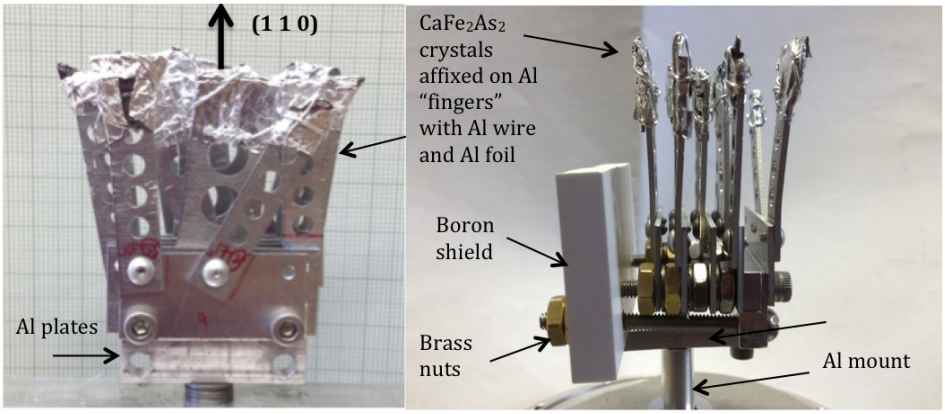

Figure 3.3 The mount for 12 co-aligned $CaFe_2As_2$ single crystals used for the experiment at ARCS, showing the experimental orientation from the front and side view. The Al mount is attached to the standard large exchange gas can at ARCS.

These fingers were attached on Al plates and mounted with a $\frac{1}{4}$" wide aluminum post mount onto the standard large exchange gas can at ARCS, as shown in Figure 3.4. The gas can is indium-sealed and helium-filled with an opening at the top for the temperature sensor mount. The maximum beam size is 2"x 2" wide as seen in the dimensions given in Figure 3.4. The sample was attached to the cold-finger of a cryostat.

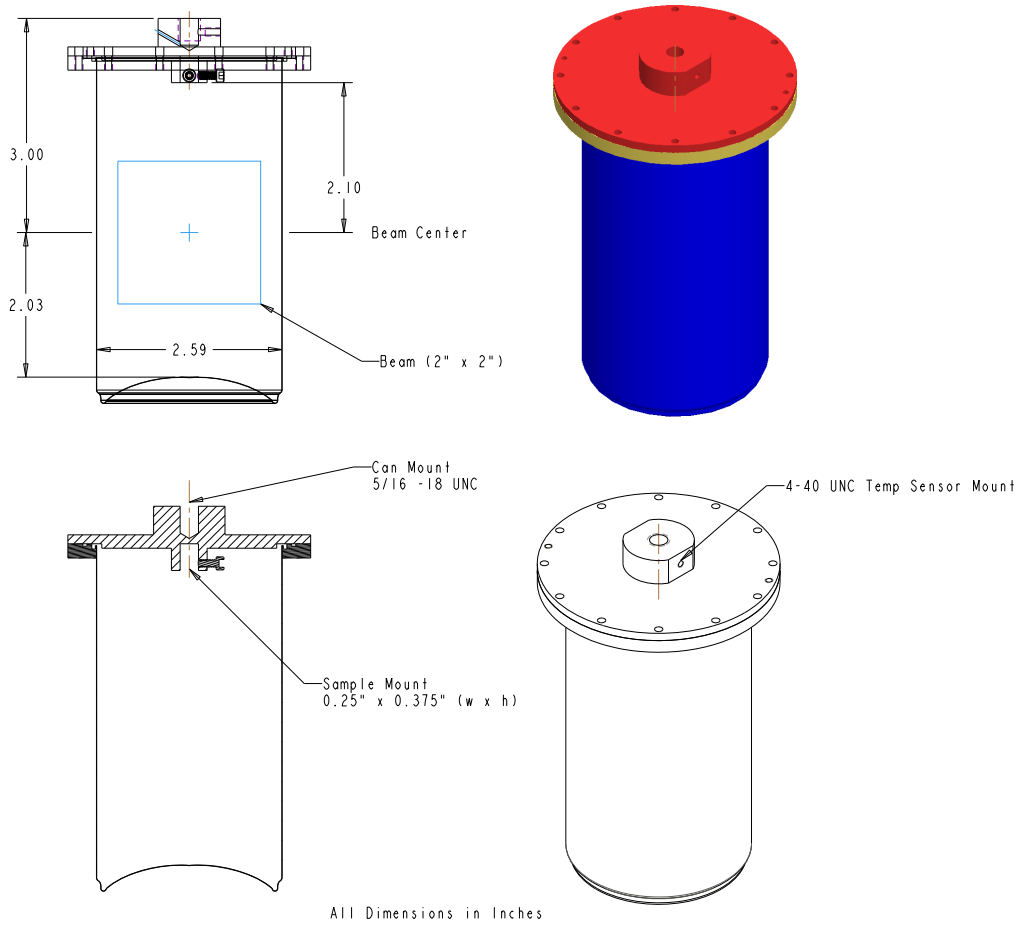

Figure 3.4 Dimensions of the standard large exchange gas can at ARCS. It is Indium sealed and filled with helium. The beam location on the can is shown in the blueprint.

3.1.2 Scattering geometry and convention

The data presented here are described in the tetragonal I4/mmm coordinate with $\mathbf{Q} = \frac{2\pi}{a}(H+K)\hat{i}+\frac{2\pi}{a}(H-K)\hat{j}+\frac{2\pi}{c}L\hat{k}$. The convention was introduced in Chapter 2. The momentum transfer can be projected into $\mathbf{Q}_{\parallel}$, in the $\hat{k}$ direction and $\mathbf{Q}_{\perp}$, in the basal plane. For antiferromagnetic wave vector, $\mathbf{Q_{AFM}} = (\frac{\mathbf{1}}{\mathbf{2}}, \frac{\mathbf{1}}{\mathbf{2}}, \mathbf{L})$, where $H = \frac{1}{2}$ and $K = 0$ and $L = odd$. H and K are defined to conveniently describe diagonal cuts in the I4/mmm basal plane as varying H corresponds to a longitudinal $[H, H]$ scan while varying K corresponds to a transverse$[K, -K]$ scan through the antiferromagnetic wave vector. It can also be shown that H and K are the reciprocal lattice vectors of the Fe square lattice as discussed by G. S. Tucker.[72]

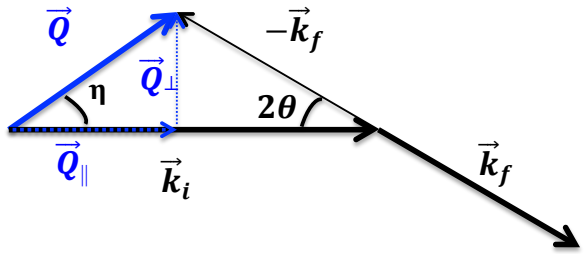

Figure 3.5 The scattering vector with incident beam $\mathbf{k_i}$ and outgoing beam $\mathbf{k_f}$. The c-axis of the sample is parallel to the incident beam

The scattering vector $\mathbf{Q}$ can be decomposed into $\mathbf{Q}_\parallel$, the component parallel to the incident energy beam, and $\mathbf{Q}_\perp$, the component perpendicular to the energy beam, as presented in Figure 3.5. From the law of cosines, and using the relationship for $cos\ \eta = \frac{\mathbf{Q}_\parallel}{\mathbf{Q}}$ one can write $\mathbf{Q}_\parallel$ as

$$Q_\parallel = k_i - \sqrt{k_i^2 - (Q_\perp^2 + k_i^2 - k_f^2)} \tag{3.1}$$

The minus sign was chosen for neutron energy loss. Using the dispersion relation and energy conservation, one can write $\mathbf{Q}_\parallel$ ($\mathbf{Q}_\perp$, E, E_i) as

$$Q_\parallel = \sqrt{\frac{2mE_i}{\hbar^2}} - \sqrt{\frac{2m(E_i - E)}{\hbar^2} - Q_\perp^2} \tag{3.2}$$

The L-component of the wave vector is modulated by the energy transfer. Hence, this calculation is important to determine the L-component of the wavevector when energy is varied at constant $\mathbf{Q}_\perp$.

3.2 Results

In these experiments, we performed a detailed survey of the spin fluctuations at temperatures above ($T = 150$ K) and below ($T = 10$ K). A white beam was first used to get 'Laue' like pattern to obtained lattice parameters, orientation and to check the alignment. The average lattice parameters found were $a = 3.9605$ Å and $c = 11.705$ Å at $T = 150$ K. The tetragonal to collapsed tetragonal (T-cT) transition is $T_S \approx 90$ K based on the lattice collapse in reference [9]. This structural transition temperature was verified with a temperature-dependent measurement of the lattice parameter c, as seen in Figure 3.6. The lattice parameter c was reduced by approximately 8.5 % from 150 K to 50 K. Magnetic scattering data were checked at various temperature to ensure a complete magnetic transition. To take accurate measurements in the collapsed phase, the low-temperature measurements were taken at $T = 10$ K, well below this transition temperature.

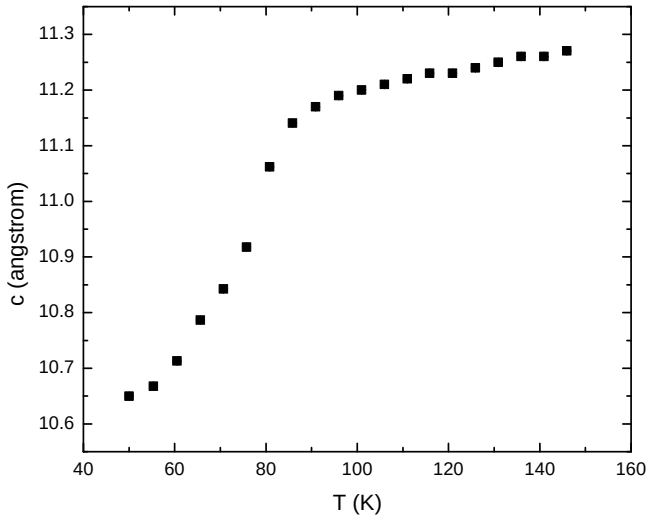

Figure 3.6 Values for the c-lattice parameter as a function of temperature,T (K) for the un-annealed, FeAs-flux as-grown $CaFe_2As_2$ sample determined from neutron diffraction measurements at ARCS. The data was collected till 40 K but was subsequently lower to 10 K to ensure a full structural transition.

The alignment and crystallinity of the sample was checked with a rocking curve of (0 0 2) peak at various temperatures and incident energies, allowing one to find the maximum and

minimum angles as the peak moves when the sample is cooled from 150 K to 10 K. The rocking curves of the peak for temperature at T = 150 K and 10 K for similar region of interest is presented in Figure 3.7. From the fitted gaussian, the FWHM at T = 150 K is 1.16 and at T = 10 K is 1.45.

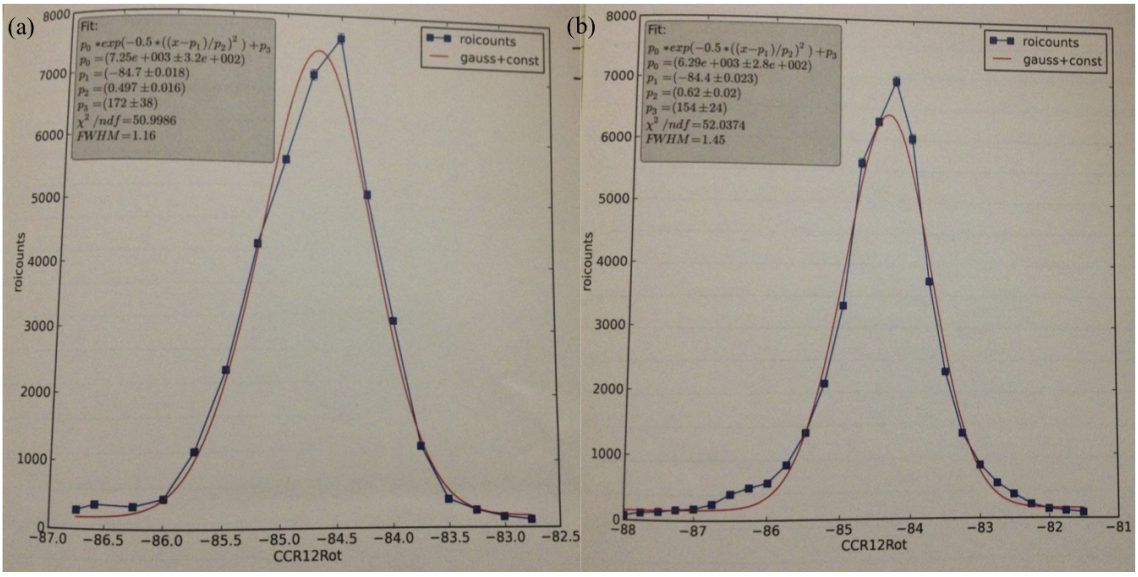

Figure 3.7 The rocking curve of (0 0 2) peak taken for incident energy, E_i = 75 meV at (a) 150 K and (b) 10 K for the same region of interest.

3.2.1 Absence of spin fluctuations in cT phase

We used MSLICE software to visualize and analyze the data.[68] All data has been normalized by the incident beam's proton charge in the reduction process. When possible, data were folded for symmetry equivalence to improve statistics. The reduction process and analysis are described in Chapter 3. One and two-dimensional cuts through the main crystallographic symmetry directions were performed for subsequent data analysis. One of the main goals is to investigate if the collapsed tetragonal phase is truly non-magnetic. Figures 3.8 and 3.9 show the two-dimensional slices taken that display the key result of our measurements.

Figures 3.8 shows constant energy transfer slices for $E_i = 75$ meV at an energy transfer of $E = 50 \pm 10$ meV [Figures 3.8(a)], and $E_i = 250$ meV at an energy transfer of $E = 80 \pm 10$ meV [Figures 3.8(b)] taken at 150 K, above the tetragonal to collapsed tetragonal transition temperature. The AFM spin fluctuations centered at $\mathbf{Q}_{AFM}$ and higher order positions (for E_i = 250 meV) are clearly observed. Figures 3.8 (c) and (d) show the neutron intensity for these same constant energy ($\Delta E = \pm$ 10meV) slices taken at $T = 10$ K in the cT phase, demonstrating the absence of magnetic scattering in the vicinity of $\mathbf{Q}_{AFM}$. We find no evidence of magnetic intensity at other positions in the zone.

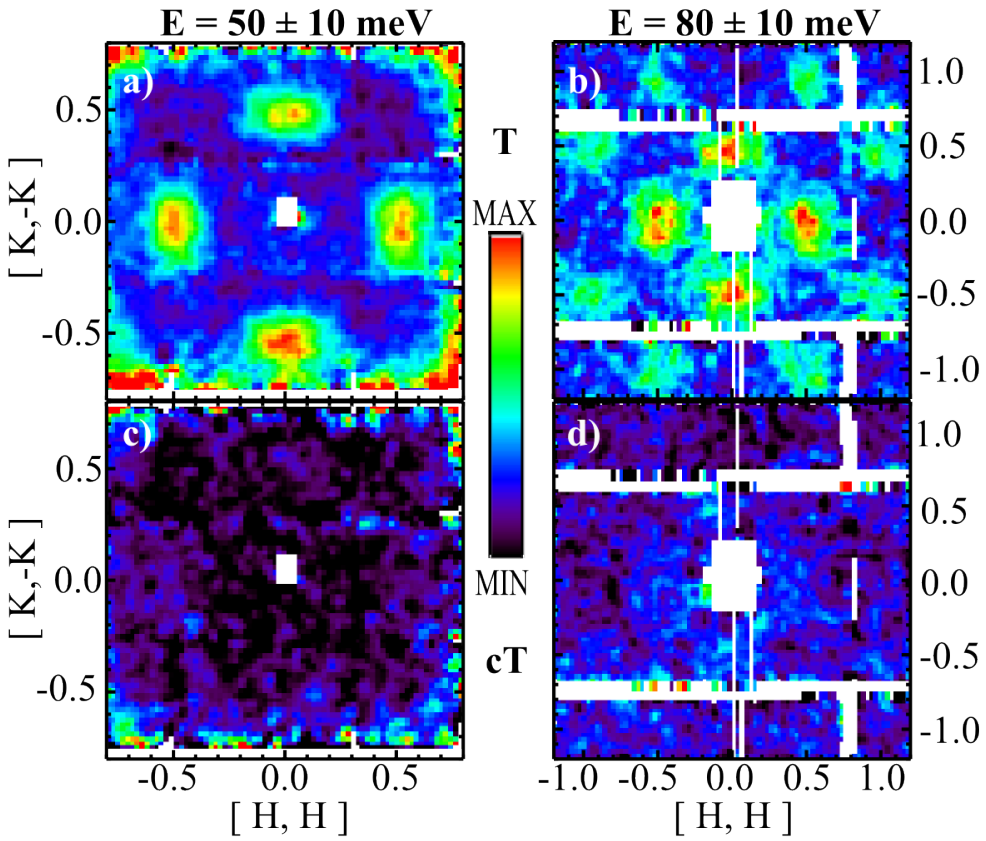

Figure 3.8 Constant energy ($\Delta E = \pm 10$ meV) slices in the (H, H) - (K, -K) plane with incident beam energies of 75 meV (left panel) and 250 meV (right panel). The color scale shows the intensity of the scattered neutrons in the stated energy intervals. The white lines are regions corresponding to gaps in the detector coverage. The paramagnetic T phase at $T = 150$ K is shown in panels (a) and (b). There is no evidence of magnetic excitations in the cT phase at $T = 10$ K in panels (c) and (d).

Figure 3.9 shows the corresponding set of energy transfer slices taken in the vicinity of $\mathbf{Q}_{AFM}$. The plots show magnetic intensity along the [K,-K] direction and energy transfer, E, after averaging over the longitudinal [H, H] direction from $0.45 < \mathrm{H} < 0.55$ in reciprocal lattice units (r.l.u). Figures 3.9 (a) and (c) show the neutron intensity for $E_i = 75$ meV and 250 meV, respectively, taken at $T = 150$ K. In the T phase, the plume of scattering at $\mathbf{Q}_{AFM}$ extends well above 100 meV [Fig. 3.9 (c)]. The transfer energy slices taken in the cT phase, at $T = 10$ K, again show no evidence of magnetic scattering in this region.

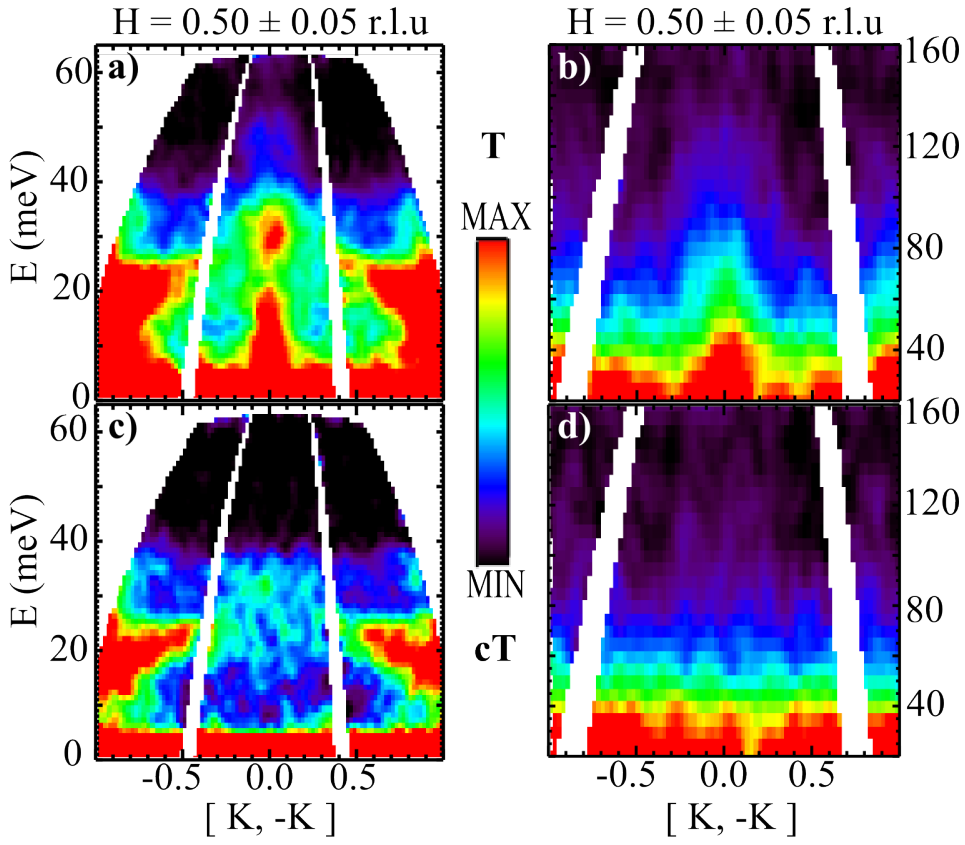

Figure 3.9 Transfer energy slices of the magnetic intensity along the [K, -K] direction after averaging over an interval of ±0.05 in the longitudinal [H, H] direction for incident energies of 75 meV (left panel) and 250 meV (right panel). In panels (a) and (b), the magnetic excitation are clearly evident, extending up to at least $E = 140$ meV in the paramagnetic T phase at $T = 150$ K for $E_i = 250$ meV. At low temperature, in the collapsed tetragonal phase, at $T = 10$ K [panels (c) and (d)], magnetic excitations are absent. The dispersing features entering from the left and right sides of panels (a) and (c) are phonons from the Al sample holder.

Implications

Figures 3.8 and 3.9 clearly demonstrate that the AFM fluctuations characteristic of the tetragonal phase are absent in the collapsed tetragonal structure, consistent with the absence of any Fe moment. The full suppression of magnetism and the absence of superconductivity in the collapsed tetragonal phase supports current theories of unconventional pairing in the iron pnictides via spin fluctuations, and raises important questions regarding the origin of superconductivity in the collapsed tetragonal phase of $(Ca_{1-x}Sr_x)Fe_2As_2$ with $T_c \approx 22$ K [46] and $(Ca_{1-x}R_x)Fe_2As_2$ (R = Pr, Nd) with $T_c > 45$ K [48]. Both References [46] and [48] acknowledge the possibility of the SC originating in a second phase, perhaps within some retained tetragonal phase as found for $CaFe_2As_2$ under uniaxial pressure.[51] On the other hand, the values for T_c in these systems is significantly higher than that found for $CaFe_2As_2$ (≈ 10 K), offering the possibility that superconductivity arises from an alternative pairing scenario. Clearly, it would be instructive to study examples of the Sr and R-substituted compounds using the time-of-flight methods described here to establish whether remnants of magnetic fluctuations persist into the cT phase.

3.2.2 Antiferromagnetic spin fluctuations in tetragonal phase

The absence of magnetic scattering in the cT phase provides us with a nonmagnetic analog for further investigations of the spin fluctuations in the higher-temperature T phase. Figure 3.10 displays the energy-dependent spin fluctuations near the antiferromagnetic wavevector in the tetragonal phase for $E_i = 75$ meV (a) and $E_i = 250$ meV (b). The observed magnetic inelastic neutron scattering data in terms of the dynamical structure factor, $S(\mathbf{Q},\omega)$, is obtained after subtracting a background function $B(\mathbf{Q},\omega)$ from the measured intensity $I(\mathbf{Q},\omega)$ ($S(\mathbf{Q},\omega) = I(\mathbf{Q},\omega)$ - $B(\mathbf{Q},\omega)$). The background is usually estimated at a vector away from the magnetic scattering features but we were able to obtain these plots by directly subtracting the data obtained in the low-temperature collapsed tetragonal phase at 10 K from the measurements in the high-temperature tetragonal phase at 150 K.

The resultant difference spectrum was folded across the the diagonals of Fig. 3.8, increasing the statistics by taking advantage of the four-fold symmetry of the (H, H)-(K, -K) plane. The range of integration in Q was H = 0.45 to 0.55 r.l.u. and K = -0.06 to +0.06 r.l.u., for consistency with Reference [54]. The intensity modulation with energy arises from variations in the structure factor along L which are observed as energy-dependent intensity oscillations that are peaked at the AFM zone centers [L = 1(≈ 10 meV), L = 3(≈ 30 meV), L = 5(≈ 50 meV)].[54]

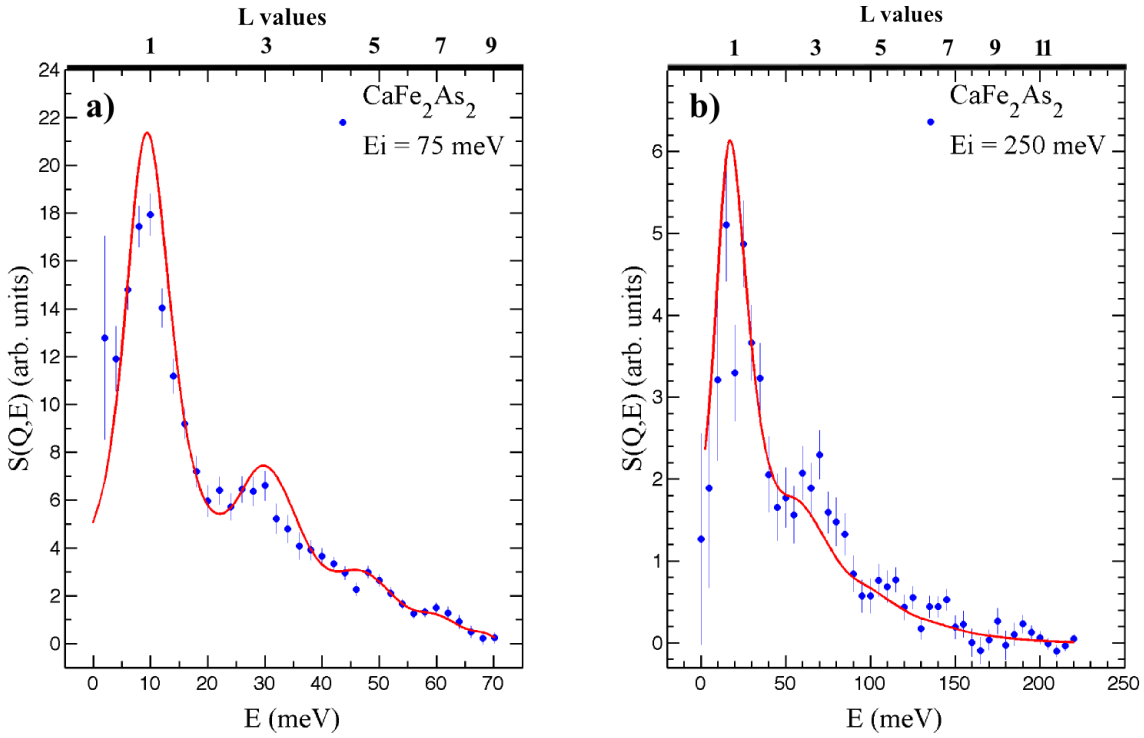

Figure 3.10 The dynamical structure factor, $S(\mathbf{Q},\omega)$, as a function of energy measured at $\mathbf{Q_{AFM}} = (\frac{1}{2},\frac{1}{2},L)$ for incident neutron energies of a) 75 meV and b) 250 meV. The scales at the top is the **L** values for corresponding energy values. The solid lines represent fits to the data as described in the text.

Background subtraction

Figure 3.11 shows a comparison of the background intensity as a function of energy around $\mathbf{Q_{AFM}}$ = (0.5, 0.5, L) for two methods, one by subtracting a non-magnetic background at off peak wave vector at T = 150 K and the second which was performed in the current studies, by subtracting the cT phase from the T phase. The comparison in figure 3.11 shows there is no additional excitation in the collapsed tetragonal phase.

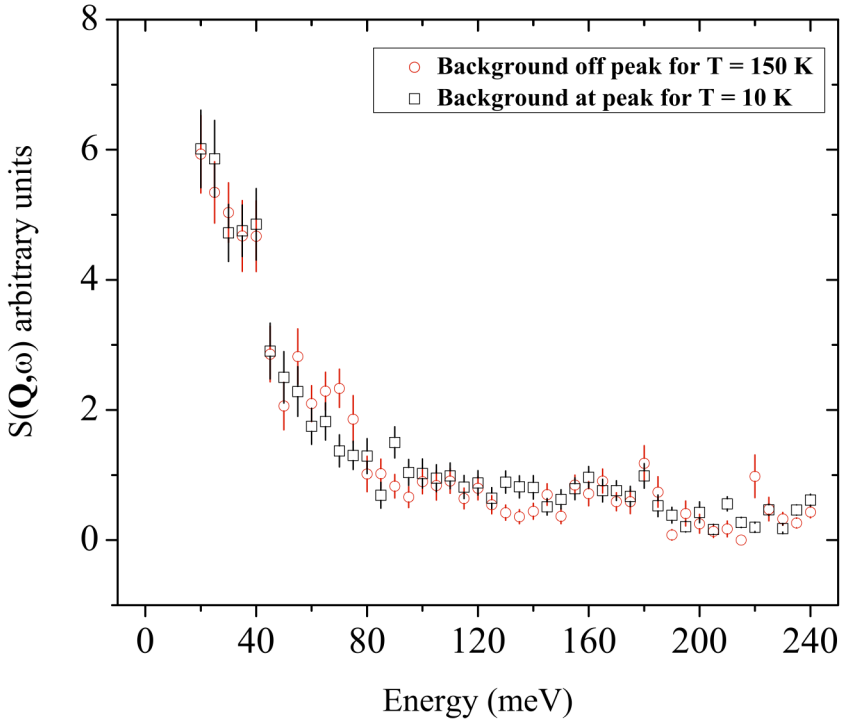

Figure 3.11 Energy dependence of the signal measured on ARCS. Open circles are background data estimated from a non-magnetic peak. Open squares show the background data obtained at the supposed magnetic peak in cT phase at T = 10 K.

Complementing these data, in Figure 3.12 we show constant-energy cuts through $\mathbf{Q}_{AFM}$ along the longitudinal [H, H] and transverse [K, -K] directions for energy transfers from 20 to 120 meV. Data taken in the paramagnetic T phase at 150 K (blue circles) are contrasted with the corresponding cuts in the cT phase at 10 K (shaded squares), once again demonstrating the absence of any magnetic signal in the cT phase. Furthermore, the background scattering away

from $\mathbf{Q_{AFM}}$ in the T phase is indistinguishable from the scattering in the cT phase indicating that there is no additional paramagnetic contribution.

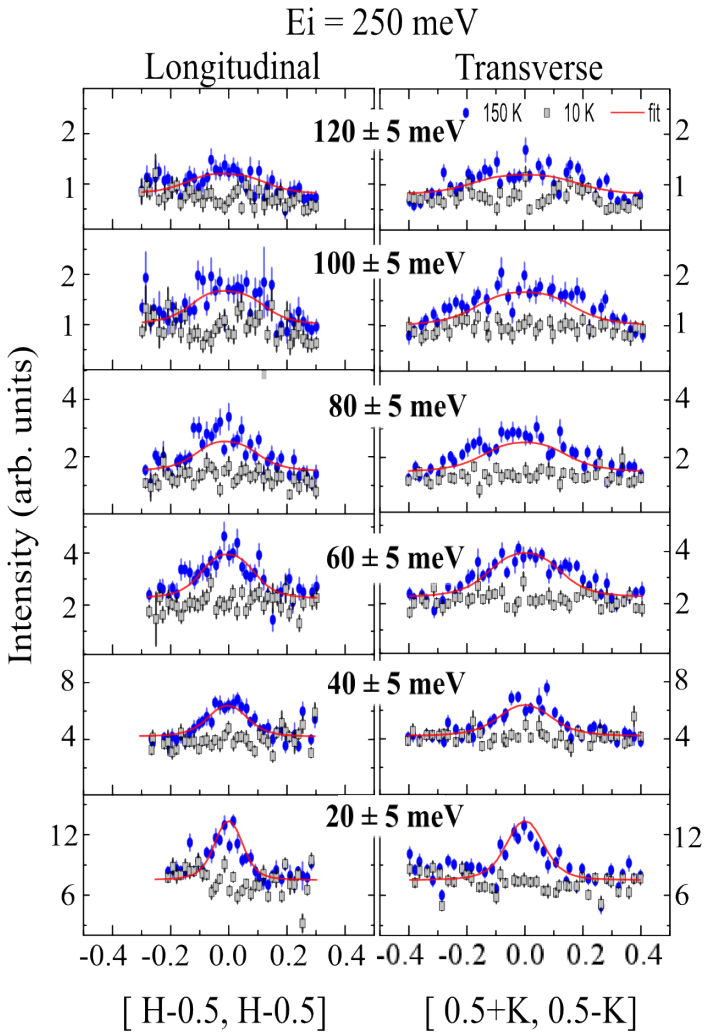

Figure 3.12 Constant-energy Q-cuts of the magnetic scattering along the longitudinal [H, H] direction (left panel) and transverse [K,-K] direction (right panel) with an incident neutron energy of 250 meV for the T phase at 150 K (blue circles) and the cT phase (shaded squares). The in-plane anisotropy of the scattering is clearly seen by comparing the widths of the scattering in the longitudinal and transverse directions at a given energy transfer. The solid lines represent fits to the data as described in the text.

Following reference [54], the transfer-energy cuts and constant-energy cuts in Figures 3.10 and 3.12 can be described by a scattering model that includes short-ranged and anisotropic

spin correlations with overdamped dynamics. The dynamic susceptibility (imaginary part) can be written as,

$$\chi''(\mathbf{Q},\omega) = \frac{\hbar\omega\gamma\chi_0}{(\hbar\omega)^2 + \gamma^2\{(q^2 + \eta q_x q_y)a^2 + (\frac{\xi_T}{a})^{-2} + \eta_c[1 + cos(\pi L)]\}^2} \tag{3.3}$$

where $\mathbf{Q} = \mathbf{Q_{AFM}} + \mathbf{q}$ and $q^2 = q_x^2 + q_y^2$. The parameter χ_0 is staggered susceptibility, ξ_T is the magnetic correlation length at temperature T in units of Å, and γ is the damping coefficient from the spin decay into particle-hole excitations. Two dimensionless parameters describe the anisotropy of the in-plane correlation lengths (η) and the strength of the interlayer spin correlations ($\eta_c = J_c\chi_0$). Here, $\gamma = \Gamma_T(\frac{\xi_T}{a})^2$, where Γ_T is the Lorentzian energy width and a is the in-plane lattice parameter. The Lorentzian width and the correlation length ξ_T are used to describe quasielastic excitation,

$$\chi''(\mathbf{Q},\omega) = \frac{\hbar\omega\Gamma_T\chi_T}{(\hbar\omega)^2 + \Gamma_T^2(1 + q^2\xi_{T+}^2)^2} \tag{3.4}$$

As mentioned, the magnetic intensity, $S(\mathbf{Q},\omega)$, is proportional to the imaginary part of the dynamic spin susceptibility $\chi''(\mathbf{Q},\omega)$ via the fluctuation-dissipation theorem,

$$S(\mathbf{Q},\omega) \propto \frac{F^2(Q)\ \chi''(\mathbf{Q},\omega)}{(1 - e^{-\hbar\omega/k_BT})} \tag{3.5}$$

where F(Q) is the Fe^{2+} magnetic form factor. The values for $\gamma = 43$ meV, $\xi_T = 7.9$ Å, $\eta = 0.55$ and $\eta_c = 0.20$ were determined for the paramagnetic T phase at 180 K in Ref. [54]. Using equation 3.4 and 3.5 along with these values, we obtain excellent fits (lines in Figures 3.10 and 3.12) to our measured data varying only a scaling constant. It should be noted that the present data set extends to much higher energies than previously measured for $CaFe_2As_2$. Therefore, this data provides additional validation of the nearly AFM spin fluctuation model proposed by

Diallo et al. and, in addition, shows that the spin dynamics of the FeAs flux-grown samples and the original Sn flux-grown samples are identical.[54] We further note that the simple diffusive response of the spin excitations in $CaFe_2As_2$ differ from what has been previously measured for the $BaFe_2As_2$ compound where a distinct transverse splitting appears in both the ordered and paramagnetic phases at high energies.[73]

Conclusion

In summary, we have studied the magnetic excitation of $CaFe_2As_2$ in the tetragonal (150 K) and collapsed tetragonal (10 K) phase for two incident energy, $E_i = 75$ meV and $E_i = 250$ meV. Our time-of-flight inelastic neutron scattering data demonstrate that the cT phase at 10 K is non-magnetic for the wide range of wave vector and energy studied. Based on an accurate background subtraction using the non-magnetic cT phase, we find no evidence for spin fluctuations at other wave vectors or any other incoherent spin fluctuations and conclude that the magnetic fluctuations are exclusive to $\mathbf{Q}_{AFM}$ for energies below 120 meV. The absence of magnetic ordering and spin fluctuations in this non-superconducting collapsed tetragonal phase supports the notion that antiferromagnetic spin fluctuations and superconductivity are intimately related. In light of recent reports of high-temperature superconductivity in the cT phase of $(Ca_{1-x}Sr_x)Fe_2As_2$ and $(Ca_{1-x}R_x)Fe_2As_2$ (R = Pr, Nd), the absence of spin fluctuations in the cT phase of $CaFe_2As_2$ calls for similar measurements on these systems.[48]

BIBLIOGRAPHY

[1] J. Paglione and Richard L. Greene. High-temperature superconductivity in iron-based materials. *Nature Physics*, 6:645–658, 2010.

[2] S. Nandi, M. G. Kim, A. Kreyssig, R. M. Fernandes, D. K. Pratt, A. Thaler, N. Ni, S. L. Bud'ko, P. C. Canfield, J. Schmalian, R. J. McQueeney, and A. I. Goldman. Anomalous suppression of the orthorhombic lattice distortion in superconducting $Ba(Fe_{1-x}Co_x)_2As_2$ single crystals. *Physical Review Letter*, 104:057006, 2010.

[3] Daniel K. Pratt. Studies of long range order and excitations in the iron arsenide superconductors. *Ph. D. thesis at Iowa State University*, Ames, USA, 2011.

[4] David C. Johnston. The puzzle of high temperature superconductivity in layered iron pnictides and chalcogenides. *Advances in Physics*, 59:803–1061, 2010.

[5] N. Ni, S. Nandi, A. Kreyssig, A. I. Goldman, E. D. Mun, S. L. Bud'ko, and P. C. Canfield. First-order structural phase transition in $CaFe_2As_2$. *Physical Review B*, 78:014523, 2008.

[6] A. Kreyssig, M. A. Green, Y. Lee, G. D. Samolyuk, P. Zajdel, J. W. Lynn, S. L. Bud'ko, M. S. Torikachvili, N. Ni, S. Nandi, J. B. Leão, S. J. Poulton, D. N. Argyriou, B. N. Harmon, R. J. McQueeney, P. C. Canfield, and A. I. Goldman. Pressure-induced volume-collapsed tetragonal phase of $CaFe_2As_2$ as seen via neutron scattering. *Physical Review B*, 78:184517, 2008.

[7] D. K. Pratt, Y. Zhao, S. A. J. Kimber, A. Hiess, D. N. Argyriou, C. Broholm, A. Kreyssig, S. Nandi, S. L. Bud'ko, and N. Ni. Suppression of antiferromagnetic spin fluctuations in the collapsed phase of $CaFe_2$ As_2. *Physical Review B*, 79(6):060510, 2009.

[8] Hervé Jobic and Doros N. Theodorou. Quasi-elastic neutron scattering and molecular dynamics simulation as complementary techniques for studying diffusion in zeolites. *Microporous and Mesoporous Materials*, 102(1–3):21–50, 5 2007.

[9] S. Ran, S. L. Bud'ko, D. K. Pratt, A. Kreyssig, M. G. Kim, M. J. Kramer, D. H. Ryan, W. N. Rowan-Weetaluktuk, Y. Furukawa, B. Roy, A. I. Goldman, and P. C. Canfield. Stabilization of an ambient-pressure collapsed tetragonal phase in $CaFe_2As_2$ and tuning of the orthorhombic-antiferromagnetic transition temperature by over 70 K via control of nanoscale precipitates. *Physical Review B*, 83:144517, 2011.

[10] Yoichi Kamihara, Takumi Watanabe, Masahiro Hirano, and Hideo Hosono. Iron-Based layered superconductor $La(O_{1-x}F_x)FeAs$ (x = 0.05−0.12) with T_c = 26 K. *Journal of the American Chemical Society*, 130:3296–3297, 2008.

[11] Hai-Hu Wen, Gang Mu, Lei Fang, Huan Yang, and Xiyu Zhu. Superconductivity at 25 K in hole-doped $(La_{1-x}Sr_x)OFeAs$. *Europhysics Letters*, 82:17009, 2008.

[12] X. H. Chen, T. Wu, G. Wu, R. H. Liu, H. Chen, and D. F. Fang. Superconductivity at 43 K in $SmFeAsO_{1-x}F_x$. *Nature*, 453:761–762, 2008.

[13] Hiroki Takahashi, Kazumi Igawa, Kazunobu Arii, Yoichi Kamihara, Masahiro Hirano, and Hideo Hosono. Superconductivity at 43 K in an iron-based layered compound $LaO_{1-x}F_xFeAs$. *Nature*, 453:376–378, 2008.

[14] Yoichi Kamihara, Hidenori Hiramatsu, Masahiro Hirano, Ryuto Kawamura, Hiroshi Yanagi, Toshio Kamiya, and Hideo Hosono. Iron-based layered superconductor: LaOFeP. *Journal of the American Chemical Society*, 128:10012–10013, 2006.

[15] J. Bardeen, L. N. Cooper, and J. R. Schrieffer. Microscopic theory of superconductivity. *Physical Review*, 106:162–164, 1957.

[16] J. Bardeen, L. N. Cooper, and J. R. Schrieffer. Theory of superconductivity. *Physical Review*, 108:1175–1204, 1957.

[17] L. Boeri, O. V. Dolgov, and A. A. Golubov. Is $LaFeAsO_{1-x}$ F_x an electron-phonon superconductor? *Physical review letters*, 101(2):026403, 2008.

[18] Ren Zhi-An, Lu Wei, Yang Jie, Yi Wei, Shen Xiao-Li, Zheng-Cai, Che Guang-Can, Dong Xiao-Li, Sun Li-Ling, Zhou Fang, and Zhao Zhong-Xian. Superconductivity at 55 K in Iron-Based F-Doped layered quaternary compound $Sm[O_{1-x}F_x]FeAs$. *Chinese Physics Letters*, 25:2215, 2008.

[19] Cao Wang, Linjun Li, Shun Chi, Zengwei Zhu, Zhi Ren, Yuke Li, Yuetao Wang, Xiao Lin, Yongkang Luo, Shuai Jiang, Xiangfan Xu, Guanghan Cao, and Zhu'an Xu. Thorium-doping-induced superconductivity up to 56 K in $Gd_{1-x}Th_xFeAsO$. *Europhysics Letters*, 83:67006, 2008.

[20] Clarina de la Cruz, Q. Huang, J. W. Lynn, Jiying Li, W. Ratcliff II, J. L. Zarestky, H. A. Mook, G. F. Chen, J. L. Luo, N. L. Wang, and Pengcheng Dai. Magnetic order close to superconductivity in the iron-based layered $LaO_{1-x}F_xFeAs$ systems. *Nature*, 453:899–902, 2008.

[21] P. Quebe, L. J. Terbuchte, and W. Jeitschko. *Journal of Alloys and Compounds*, 302(70), 2000.

[22] Athena S. Sefat, Ashfia Huq, Michael A. McGuire, Rongying Jin, Brian C. Sales, David Mandrus, Lachlan M. D. Cranswick, Peter W. Stephens, and Kevin H. Stone. Superconductivity in $LaFe_{1-x}Co_xAsO$. *Physical Review B*, 78:104505, 2008.

[23] Alexander L. Ivanovskii. New high-temperature superconductors based on rare-earth and transition metal oxyarsenides and related phases: synthesis, properties and simulations. *Physics-Uspekhi*, 51(12):1229

[24] Zhi-An Ren, Guang-Can Che, Xiao-Li Dong, Jie Yang, Wei Lu, Wei Yi, Xiao-Li Shen, Zheng-Cai Li, Li-Ling Sun, Fang Zhou, and Zhong-Xian Zhao. Superconductivity and phase diagram in iron-based arsenic-oxides $ReFeAsO_{1-\delta}$ (Re = rare-earth metal) without fluorine doping. *Europhysics Letters*, 83:17002, 2008.

[25] Joshua H. Tapp, Zhongjia Tang, Bing Lv, Kalyan Sasmal, Bernd Lorenz, Paul C. W. Chu, and Arnold M. Guloy. LiFeAs: An intrinsic FeAs-based superconductor with $T_c = 18$ K. *Physical Review B*, 78:060505, 2008.

[26] Fong-Chi Hsu, Jiu-Yong Luo, Kuo-Wei Yeh, Ta-Kun Chen, Tzu-Wen Huang, Phillip M. Wu, Yong-Chi Lee, Yi-Lin Huang, Yan-Yi Chu, Der-Chung Yan, and Maw-Kuen Wu. Superconductivity in the PbO-type structure α-FeSe. *Proceedings of the National Academy of Sciences*, 105:14262–14264, 2008.

[27] Kenji Ishida, Yusuke Nakai, and Hideo Hosono. To what extent iron-pnictide new superconductors have been clarified: A progress report. *Journal of the Physical Society of Japan*, 78(6):062001, 2009.

[28] Marianne Rotter, Marcus Tegel, and Dirk Johrendt. Superconductivity at 38 K in the iron arsenide $(Ba_{1-x}K_x)Fe_2As_2$. *Physical Review Letter*, 101:107006, 2008.

[29] L. J. Li, Y. K. Luo, Q. B. Wang, H. Chen, Z. Ren, Q. Tao, Y. K. Li, X. Lin, M. He, Z. W. Zhu, G. H. Cao, and Z. A. Xu. Superconductivity induced by Ni doping in $BaFe_2A_2$ single crystals. *New Journal of Physics*, 11:025008, 2009.

[30] S. Kasahara, K. Hashimoto, R. Okazaki, H. Shishido, M. Yamashita, K. Ikada, S. Tonegawa, N. Nakata, Y. Sensyu, H. Takeya, K. Hirata, T. Shibauchi, T. Terashima, and Y. Matsuda. Superconductivity induced by isovalent doping in single crystals of $BaFe_2(As_{1-x}P_x)$. *Physica C: Superconductivity*, 470:S462–S463, 2010.

[31] G. Wu, H. Chen, T. Wu, Y. L. Xie, Y. J. Yan, R. H. Liu, X. F. Wang, J. J. Ying, and X. H. Chen. Different resistivity response to spin-density wave and superconductivity at 20 K in $Ca_{1-x}Na_xFe_2As_2$. *Journal of Physics: Condensed Matter Condensed Matter*, 20(42):5, October 2008.

[32] P. C. Canfield, S. L. Bud'ko, N. Ni, A. Kreyssig, A. I. Goldman, R. J. McQueeney, M. S. Torikachvili, D. N. Argyriou, G. Luke, and W. Yu. Structural, magnetic and superconducting phase transitions in $CaFe_2As_2$ under ambient and applied pressure. *Physica C: Superconductivity*, 469(9–12):404–412, May 2009.

[33] A. I. Goldman, D. N. Argyriou, B. Ouladdiaf, T. Chatterji, A. Kreyssig, S. Nandi, N. Ni, S. L. Bud'ko, P. C. Canfield, and R. J. McQueeney. Lattice and magnetic instabilities in $CaFe_2As_2$: A single-crystal neutron diffraction study. *Physical Review B*, 78:100506, 2008.

[34] Jun Zhao, W. Ratcliff, J. W. Lynn, G. F. Chen, J. L. Luo, N. L. Wang, Jiangping Hu, and Pengcheng Dai. Spin and lattice structures of single-crystalline $SrFe_2As_2$. *Physical Review B*, 78:140504, 2008.

[35] Q. Huang, Y. Qiu, Wei Bao, M. A. Green, J. W. Lynn, Y. C. Gasparovic, T. Wu, G. Wu, and X. H. Chen. Neutron-diffraction measurements of magnetic order and a structural transition in the parent $BaFe_2As_2$ compound of FeAs-based high-temperature superconductors. *Physical Review Letter*, 101:257003, 2008.

[36] D. M. Wang, X. C. Shangguan, J. B. He, L. X. Zhao, Y. J. Long, P. P. Wang, and L. Wang. Superconductivity at 35.5 K in K-doped $CaFe_2As_2$. *Journal of Superconductivity and Novel Magnetism*, pages 1–4 1557–1939, 2013.

[37] Neeraj Kumar, R. Nagalakshmi, R. Kulkarni, P. L. Paulose, A. K. Nigam, S. K. Dhar, and A. Thamizhavel. Anisotropic magnetic and superconducting properties of $CaFe_{2-x}Co_xAs_2$ (x=0, 0.06) single crystals. *Physical Review B*, 79:012504, 2009.

[38] Yanpeng Qi, Zhaoshun Gao, Lei Wang, Xianping Zhang, Dongliang Wang, Chao Yao, Chunlei Wang, Chengduo Wang, and Yanwei Ma. Superconductivity at 22 K in Ir-doped $CaFe_{2-x}Ir_xAs_2$ single crystals. *Europhysics Letters*, 96:47005, 2011.

[39] Bing Lv, Liangzi Deng, Melissa Gooch, Fengyan Wei, Yanyi Sun, James K Meen, Yu-Yi Xue, Bernd Lorenz, and Ching-Wu Chu. Unusual superconducting state at 49 K in electron-doped $CaFe_2As_2$ at ambient pressure. *Proceedings of the National Academy of Sciences*, 108(38):15705–15709

[40] Milton S. Torikachvili, Sergey L. Bud'ko, N. Ni, and Paul C. Canfield. Pressure induced superconductivity in $CaFe_2As_2$. *Physical review letters*, 101(5):057006, 2008.

[41] Tuson Park, Eunsung Park, Hanoh Lee, T. Klimczuk, E. D. Bauer, F. Ronning, and J. D. Thompson. Pressure-induced superconductivity in $CaFe_2As_2$. *Journal of Physics: Condensed Matter*, 20(32):322204 0953–8984, 2008.

[42] Patricia L. Alireza, Y. T. Ko, Jack Gillett, Chiara M. Petrone, Jacqueline M. Cole, Suchitra E. Sebastian, and Gilbert G. Lonzarich. Superconductivity up to 29 k in $SrFe_2As_2$ and $BaFe_2As_2$ at high pressures. *arXiv preprint arXiv:0807.1896*, 2008.

[43] W. Yu, A. A. Aczel, T. J. Williams, S. L. Bud'ko, N. Ni, P. C. Canfield, and G. M. Luke. Absence of superconductivity in single-phase $CaFe_2As_2$ under hydrostatic pressure. *Physical Review B*, 79(2):020511–, 01 2009.

[44] S. Kasahara, T. Shibauchi, K. Hashimoto, Y. Nakai, H. Ikeda, T. Terashima, and Y. Matsuda. Abrupt recovery of fermi-liquid transport following the collapse of the c-axis in $CaFe_2(As_{1-x}P_x)_2$ single crystals. *Physical Review B*, 83(6):060505–, 02 2011.

[45] Masataka Danura, Kazutaka Kudo, Yoshihiro Oshiro, Shingo Araki, Tatsuo C. Kobayashi, and Minoru Nohara. Interplay of superconductivity and fermi-liquid transport in Rh-doped $CaFe_2As_2$ with lattice-collapse transition. *Journal of the Physical Society of Japan*, 80:103701, 2011.

[46] J. R. Jeffries, N. P. Butch, K. Kirshenbaum, S. R. Saha, G. Samudrala, S. T. Weir, Y. K. Vohra, and J. Paglione. Suppression of magnetism and development of superconductivity within the collapsed tetragonal phase of $Ca_{0.67}Sr_{0.33}Fe_2As_2$ under pressure. *Physical Review B*, 85(18):184501–, 05 2012.

[47] Yanpeng Qi, Zhaoshun Gao, Lei Wang, Dongliang Wang, Xianping Zhang, Chao Yao, Chunlei Wang, Chengduo Wang, and Yanwei Ma. Transport properties and anisotropy in rare-earth doped cafe2as2 single crystals with tc above 40 k. *Superconductor Science and Technology*, 25(4):045007 0953–2048, 2012.

[48] S. R. Saha, N. P. Butch, T. Drye, J. Magill, S. Ziemak, K. Kirshenbaum, P. Y. Zavalij, J. W. Lynn, and J. Paglione. Structural collapse and superconductivity in rare-earth-doped $CaFe_2As_2$. *Physical Review B*, 85:024525, 2012.

[49] Zhaoshun Gao, Yanpeng Qi, Lei Wang, Dongliang Wang, Xianping Zhang, Chao Yao, Chunlei Wang, and Yanwei Ma. Synthesis and properties of la-doped cafe2as2 single crystals with tc= 42.7 k. *EPL (Europhysics Letters)*, 95(6):67002

[50] Kazutaka Kudo, Keita Iba, Masaya Takasuga, Yutaka Kitahama, Jun-ichi Matsumura, Masataka Danura, Yoshio Nogami, and Minoru Nohara. Emergence of superconductivity at 45 K by lanthanum and phosphorus co-doping of $CaFe_2As_2$. *Scientific reports*, 3, 2013.

[51] K. Prokeš, A. Kreyssig, B. Ouladdiaf, D. K. Pratt, N. Ni, S. L. Bud'ko, P. C. Canfield, R. J. McQueeney, D. N. Argyriou, and A. I. Goldman. Evidence from neutron diffraction for superconductivity in the stabilized tetragonal phase of $CaFe_2As_2$ under uniaxial pressure. *Physical Review B*, 81:180506, 2010.

[52] A. D. Christianson, E. A. Goremychkin, R. Osborn, S. Rosenkranz, M. D. Lumsden, C. D. Malliakas, I. S. Todorov, H. Claus, D. Y. Chung, and M. G. Kanatzidis. Unconventional superconductivity in $Ba_{0.6}K_{0.4}Fe_2As_2$ from inelastic neutron scattering. *Nature*, 456(7224):930–932

[53] M. D. Lumsden and A. D. Christianson. Magnetism in Fe-based superconductors. *Journal of Physics: Condensed Matter*, 22:203203, 2010.

[54] S. O. Diallo, D. K. Pratt, R. M. Fernandes, Wei Tian, J. L. Zarestky, M. Lumsden, T. G. Perring, C. L. Broholm, Ni Ni, and S. L. Bud'ko. Paramagnetic spin correlations in $CaFe_2As_2$ single crystals. *Physical Review B*, 81(21):214407, 2010.

[55] H Luetkens, H-H Klauss, M Kraken, FJ Litterst, T Dellmann, R Klingeler, C Hess, R Khasanov, A Amato, and C Baines. The electronic phase diagram of the lao1 xfxfeas superconductor. *Nature materials*, 8(4):305–309

[56] T. Goko, A. A. Aczel, E. Baggio-Saitovitch, S. L. Bud'ko, P. C. Canfield, J. P. Carlo, G. F. Chen, Pengcheng Dai, A. C. Hamann, W. Z. Hu, H. Kageyama, G. M. Luke, J. L. Luo, B. Nachumi, N. Ni, D. Reznik, D. R. Sanchez-Candela, A. T. Savici, K. J. Sikes, N. L. Wang, C. R. Wiebe, T. J. Williams, T. Yamamoto, W. Yu, and Y. J. Uemura. Supercon-

ducting state coexisting with a phase-separated static magnetic order in (Ba,K)Fe_2As_2, (Sr,Na)Fe_2As_2, and $CaFe_2As_2$. *Physical Review B*, 80(2):024508–, 07 2009.

[57] Masatoshi Arai and K Crawford. *Neutron sources and facilities*, pages 13–30 Springer, 2009.

[58] Stephen W. Lovesey. *Theory of neutron scattering from condensed matter*, volume 2, Oxford, Great Britain. 1984.

[59] Gen Shirane, Stephen M. Shapiro, and John M. Tranquada. *Neutron scattering with a triple-axis spectrometer*, volume Cambridge, Great Britain. 2002.

[60] Tapan Chatterji. *Neutron scattering from magnetic materials*, volume Amsterdam, Netherlands. 2006.

[61] R. A. Ewings, T. G. Perring, R. I. Bewley, T. Guidi, M. J. Pitcher, D. R. Parker, S. J. Clarke, and A. T. Boothroyd. High-energy spin excitations in $BaFe_2As_2$ observed by inelastic neutron scattering. *Physical Review B*, 78(22):220501, 2008.

[62] K. Matan, R. Morinaga, K. Iida, and T. J. Sato. Anisotropic itinerant magnetism and spin fluctuations in $BaFe_2As_2$: A neutron scattering study. *Physical Review B*, 79:054526, 2009.

[63] Jun Zhao, Dao-Xin Yao, Shiliang Li, Tao Hong, Y Chen, S Chang, II W Ratcliff, JW Lynn, HA Mook, and GF Chen. Low energy spin waves and magnetic interactions in $srfe_2$ as_2. *Physical review letters*, 101(16):167203, 2008.

[64] R. A. Ewings, T. G. Perring, Jack Gillett, S. D. Das, S. E. Sebastian, A. E. Taylor, Tatiana Guidi, and A. T. Boothroyd. Itinerant spin excitations in $SrFe_2As_2$ measured by inelastic neutron scattering. *Physical Review B*, 83(21):214519, 2011.

[65] Douglas L. Abernathy, Matthew B. Stone, M. J. Loguillo, M. S. Lucas, O. Delaire, Xiaoli Tang, J. Y. Y. Lin, and B. Fultz. Design and operation of the wide angular-range chopper spectrometer arcs at the spallation neutron source. *Review of Scientific Instruments*, 83(1):015114–015114–11 0034–6748, 2012.

[66] Oakridge national laboratory neutron sciences - instuments support: Neutron choppers, July 2013.

[67] Jon Taylor, O. Arnold, J. Bilheaux, A. Buts, S. Campbell, M. Doucet, N. Draper, R. Fowler, M. Gigg, and V. Lynch. Mantid, a high performance framework for reduction and analysis of neutron scattering data. *Bulletin of the American Physical Society*, 57, 2012.

[68] Radu Coldea. *Mslice* data visualization software.

[69] T. G. Worlton, A. Chatterjee, J. P. Hammonds, P. F. Peterson, D. J. Mikkelson, and R. L. Mikkelson. User software for the next generation. *arXiv preprint cs/0210018*, 2002.

[70] P. F. Peterson, Th. Proffen, R. L. Mikkelson, T. Kozlowski, DJ Mikkelson, G. Cooper, and T. G. Worlton. Sharing data between facilities: using the nexus time-of-flight powder diffractometer file format. *arXiv preprint cond-mat/0210425*, 2002.

[71] A. I. Goldman, A. Kreyssig, K. Prokeš, D. K. Pratt, D. N. Argyriou, J. W. Lynn, S. Nandi, S. A. J. Kimber, Y. Chen, Y. B. Lee, G. Samolyuk, J. B. Leão, S. J. Poulton, S. L. Bud'ko, N. Ni, P. C. Canfield, B. N. Harmon, and R. J. McQueeney. Lattice collapse and quenching of magnetism in $CaFe_2As_2$ under pressure: A single-crystal neutron and x-ray diffraction investigation. *Physical Review B*, 79:024513, 2009.

[72] G. S. Tucker, D. K. Pratt, M. G. Kim, S. Ran, A. Thaler, G. E. Granroth, K. Marty, W. Tian, J. L. Zarestky, M. D. Lumsden, S. L. Bud'ko, P. C. Canfield, A. Kreyssig, A. I. Goldman, and R. J. McQueeney. Competition between stripe and checkerboard magnetic instabilities in Mn-doped $BaFe_2As_2$. *Physical Review B*, 86:020503, 2012.

[73] L. W. Harriger, H. Q. Luo, M. S. Liu, C. Frost, J. P. Hu, M. R. Norman, and Pengcheng Dai. Nematic spin fluid in the tetragonal phase of $BaFe_2As_2$. *Physical Review B*, 84(5):054544–, 08 2011.